Available online at www.sciencedirect.com
SCIENCE DIRECT®

Dynamics of Atmospheres and Oceans
39 (2005) 103–135

dynamics of atmospheres and oceans

www.elsevier.com/locate/dynatmoce

Subsurface influence on SST in the tropical Indian Ocean: structure and interannual variability

Suryachandra A. Rao *, Swadhin K. Behera

Institute for Global Change Research, Frontier Research System for Global Change, 3173-25 Showamachi, Kanazawa-ku, Yokohama, Kanagawa 236-0001, Japan

Received 5 December 2003; accepted 5 October 2004
Available online 5 February 2005

Abstract

Interannual variations of subsurface influence on SST in the Indian Ocean show strong seasonality. The subsurface influence on SST confines to the southern Indian Ocean (SIO) in boreal winter and spring; it is observed on both sides of the equator in boreal summer and fall. Interannual long Rossby waves are at the heart of this influence, and contribute significantly to the coupled climate variability in the tropical Indian Ocean (TIO). Principal forcing mechanism for the generation of these interannual waves in the Indian Ocean and the relative influence of two dominant interannual signals in the tropics, namely El Niño and Southern Oscillation (ENSO) and Indian Ocean Dipole (IOD), are also discussed. Two distinct regions dominated by either of the above climate signals are identified. IOD dominates the forcing of the off-equatorial Rossby waves, north of 10°S, and the forcing comes mainly from the anomalous Ekman pumping associated with the IOD. However, after the demise of IOD activity by December, Rossby waves are dominantly forced by ENSO, particularly south of 10°S.

It is found that the subsurface feedback in the northern flank of the southern Indian Ocean ridge region (north of 10°S) significantly influences the central east African rainfall in boreal fall. The Indian Ocean coupled process further holds considerable capability of predicting the east African rainfall by one season ahead. Decadal modulation of the subsurface influence is also noticed during the study period. The subsurface influence north of 10°S coherently varies with the IOD, while it varies coherently with the ENSO south of this latitude.

Keywords: Indian Ocean Dipole; El Niño and Southern Oscillation; Indian Ocean; Ocean dynamics

* Corresponding author. Tel.: +81 45 778 5520; fax: +81 45 778 5707.
E-mail address: scrao@jamstec.go.jp (S.A. Rao).

0377-0265/$ – see front matter © 2004 Elsevier B.V. All rights reserved.
doi:10.1016/j.dynatmoce.2004.10.014

1. Introduction

El Niño and Southern Oscillation (ENSO), a distinct ocean–atmospheric coupled phenomenon in the tropical Pacific, is a clear example of emphasizing the influence of subsurface on SST and therefore to the atmosphere (Bjerknes, 1969; Neelin et al., 1998 and references therein). This coupled phenomenon is believed to be the strongest climate modulator in the tropics on interannual time scale. The wide-spread impact of this phenomenon on the global climate is emphasized in several studies (e.g. Wallace et al., 1998; Trenberth et al., 1998 and references therein). Decadal variability of this coupled phenomenon is also well documented in the literature (e.g. An and Wang, 2000; Trenberth and Hurrell, 1994).

Although the understanding of the tropical Pacific phenomenon has been deepened in the past decades, the coupled process studies in the tropical Indian Ocean (TIO) are very limited partly owing to the belief that the Indian Ocean climate simply responds to changes in the tropical Pacific climate (e.g. Latif and Barnett, 1995; Venzke et al., 2000) and partly owing to the lack of sufficient observations. However, after the discovery of the Indian Ocean Dipole (IOD) (Saji et al., 1999), the interannual ocean–atmosphere coupled variability has received unprecedented attention (Vinayachandran et al., 1999; Behera et al., 1999; Iizuka et al., 2000; Murtugudde et al., 2000; Schiller et al., 2000; Rao et al., 2002a,b; Ashok et al., 2001; Guan et al., 2003). Studies of teleconnection patterns associated with this phenomenon are evolving in the recent literature (Behera et al., 1999; Ashok et al., 2001, 2003; Larref et al., 2003; Saji and Yamagata, 2003a,b; Guan and Yamagata, 2003). It is known from the previous literature that IOD phenomenon is seasonally phase-locked; the IOD evolves in summer, peaks in the fall and decays in the winter (Saji et al., 1999). The exact nature of subsurface influence on SST and its seasonal dependence are, however, still need to be pursued.

Several studies also looked at the subsurface interannual variability in the Indian Ocean and related it to either IOD (Rao et al., 2002a,b; Vinayachandran et al., 2002) or ENSO (Tourre and White, 1995; Chambers et al., 1999; Xie et al., 2002). One of the important findings is the role of Rossby waves in maintaining the IOD during its evolution and peak phases (Webster et al., 1999; Murtugudde et al., 2000) and also during turnabout from positive (negative) to negative (positive) IOD events (Rao et al., 2002a). However, roles of these waves in influencing the SST and how these waves are forced interannually are not fully investigated in the existing literature.

There are several studies on the detection of long Rossby waves in the TIO. Most of them examined annual and semi-annual periodicities in selected regions, such as the Bay of Bengal (Kumar and Unnikrishna, 1995; Rao, 1998), the equatorial Indian Ocean (Yamagata et al., 1996; Le Blanc and Boulanger, 2001), and the southern Indian Ocean (SIO) (Woodberry et al., 1989; Perigaud and Delecluse, 1992; Masumoto and Meyers, 1998). These previous studies clarified that the Rossby waves with annual periodicity are dominant in the SIO (Woodberry et al., 1989; Perigaud and Delecluse, 1992; Masumoto and Meyers, 1998) and semi-annual as well as annual period Rossby waves are dominant in the equatorial Indian Ocean (Yamagata et al., 1996) and in the Bay of Bengal (Rao, 1998).

Rossby waves with interannual periodicity (3–5 years) are also identified in the SIO (Perigaud and Delecluse, 1993; Masumoto and Meyers, 1998; Chambers et al., 1999).

Furthermore, Masumoto and Meyers (1998) showed that these waves are primarily forced by the wind stress curl along the Rossby wave path. Recently, Xie et al. (2002) (hereafter X02) studied the interannual variability in the SIO and showed that Rossby waves in the region between 8°S and 12°S are very important in air–sea coupling in the SIO. X02 also claimed that the air–sea coupling in this region is closely linked with the Pacific ENSO rather than the IOD. They noted that ENSO-forced off-equatorial Rossby waves are prominent only in the SIO but not in the northern Indian Ocean (NIO). Fig. 1 shows the correlation of sea surface temperature anomalies (SSTA) with sea surface height anomalies (SSHA) and depth of 20 °C isotherm depth anomalies (D20A). Box surrounded by thick black line represents the study region of X02. Since open-ocean upwelling and associated thermocline feedback spread to a wider region in SIO beyond the study of X02 (Fig. 1b), X02's study region between 8°S and 12°S is not enough. Masumoto and Meyers (1998) also restricted their study region to a relatively narrow region in the SIO. Therefore, we study here the interannual Rossby waves in the NIO and in the other regions of SIO. Decadal modulation of subsurface influence on SST is also of interest in the TIO.

Here in this article, after describing the data and methods in Section 2, we show structure of the subsurface influence on SST in the TIO and its seasonal dependence in Section 3. Interannual variability associated with this subsurface influence is pursued in Section 4. Forcing mechanisms of the Rossby wave signals that are involved in the subsurface influence are described in Section 5. Impact of this influence on east African rainfall is discussed in Section 6. The decadal modulation of the influence is described in Section 7. Section 8 summarizes the results of the present study.

2. Data and methodology

The primary dataset used for the present study is the simple ocean data assimilation (SODA) product (Carton et al., 2000). In this data assimilation project, Carton et al. (2000) use an ocean general circulation model Modular Ocean Model (MOM 2.0) to interpolate observed fields of temperature, salinity, and currents to regular grids at regular time intervals. We also use comprehensive ocean–atmosphere dataset (COADS) winds from 1950 to 1992 and National Center for Environmental Prediction-National Center for Atmospheric Research (NCEP-NCAR) re-analysis monthly winds (Kalnay et al., 1996) from 1993 to 1999 in correspondence with the wind stress forcing used in SODA. X02 introduced an ENSO index to represent the ENSO variability and a Sumatra index to represent the Indian Ocean coupled variability. The ENSO index is defined as the SST anomalies averaged in the region of 180°W–140°W and 3°S–3°N for October–December; Sumatra index is defined as the SST anomalies for September–November averaged in the region of 90°E–100°E and 10°S–equator. The Sumatra index is highly correlated ($r = 0.9$) with the dipole mode index (DMI) defined by Saji et al. (1999). This high correlation indicates that the original DMI proposed by Saji et al. (1999) for SON season is sufficient enough to document the interannual variability in the Indian Ocean. However, we use the same indices employed in X02 to represent ENSO and Indian Ocean variability to facilitate comparison of results. Sumatra index is slightly modified to include the whole region of eastern box (90°E–110°E; 10°S–equator) as in Saji et al. (1999). This whole region is found to be very important region

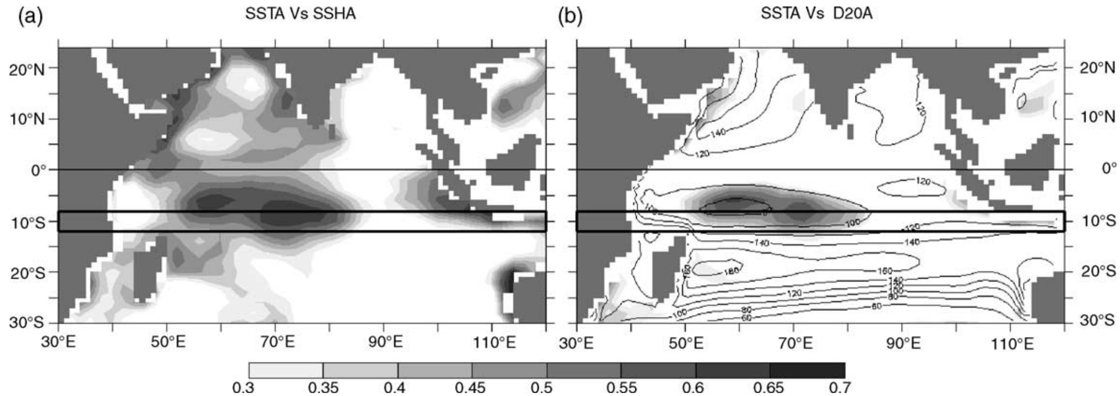

Fig. 1. Correlation between SST anomalies and (a) SSH anomalies, (b) D20 anomalies. Annual mean D20 contours are overland.

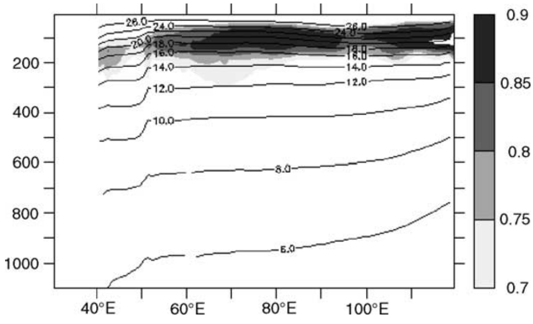

Fig. 2. Correlation between SSH anomalies and temperature anomalies along 10°S in the tropical Indian Ocean. Annual mean isotherms are overlaid.

for initiation (Annamalai et al., 2003) and termination of Indian Ocean Dipole (Rao and Yamagata, 2004).

In this study, we prefer to use sea surface height (SSH) derived from SODA, rather than a particular depth of isotherm, to identify the thermocline depth. In general, the thermocline depth is defined as the depth where maximum temperature gradient occurs in a temperature profile. Considering the vertical resolution of the SODA dataset (which is 15 m in the upper ocean), it is very difficult to estimate the thermocline depth accurately. Nevertheless, we estimate the depth of maximum temperature gradient and correlate it with both D20A and SSHA; higher correlation coefficients are found with SSHA (not shown). This distinction between using SSHA over D20A is clearly evident in Fig. 1. Correlation of SSHA with SSTA shows better correlation in regions where D20A do not show any significant correlation. We also correlate the SSHA with temperature anomalies at different depths along different latitudinal belts, and found correlation maxima in the thermocline (Fig. 2).[1] Further, the depth distribution of both maximum temperature gradient and D20, derived from the SODA data, is not smooth over the entire basin owing to the coarse vertical resolution. Therefore, the SSH is preferred to depth of a particular isotherm.

The results obtained using SSH and D20 are similar, except that the peak correlation coefficients are slightly higher with SSH by order of 0.1 both for ENSO and Sumatra indices. Although the ENSO and Sumatra indices have been derived from the primary dataset SODA, we also cross-checked our results with GISST (Rayner et al., 1996) and also with NCEP/NCAR re-analysis dataset (Kalnay et al., 1996). The results from these different datasets are in good agreement with those using SODA.

3. Seasonality of the subsurface influence on SST in the TIO

As the dynamics and thermodynamics in TIO exhibit strong seasonal variations (Schott and McCreary, 2001 and references therein), logically it is reasonable to look at the sub-

[1] Only 10°S zonal belt correlations are shown in Fig. 2. Other zonal belts also show correlation coefficients of the same order.

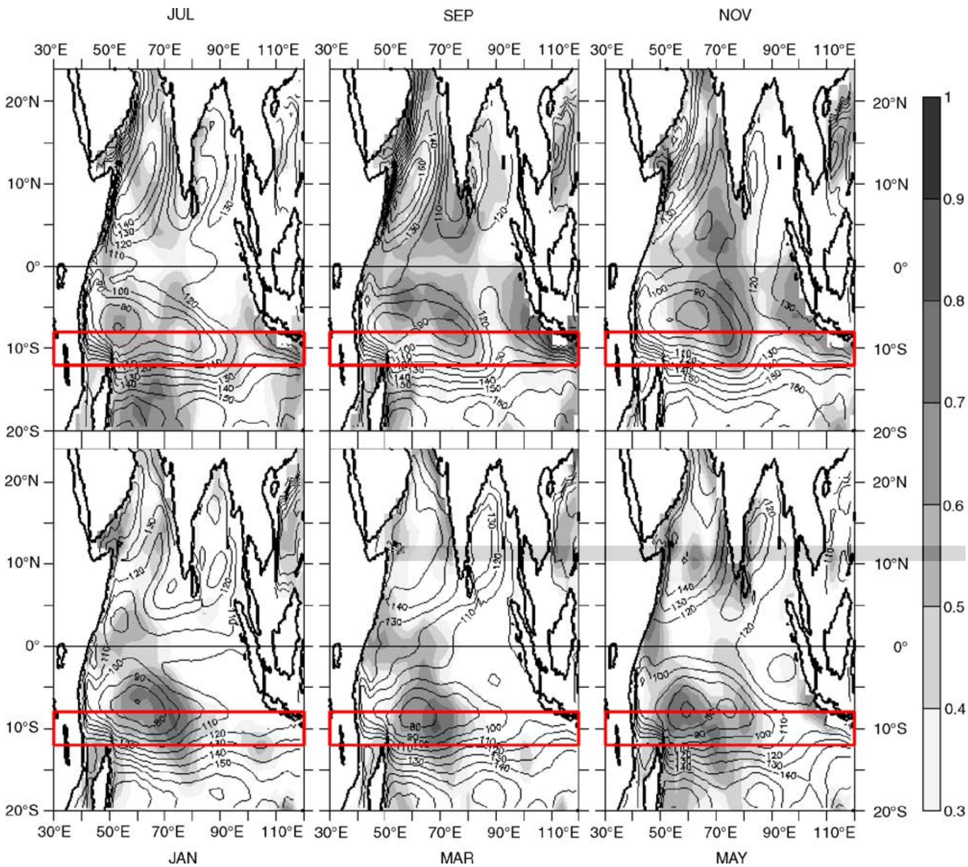

Fig. 3. Seasonal cycle of the interannual thermocline feedback in the tropical Indian Ocean represented as the correlation between SSH anomalies and SST anomalies for respective months.

surface influence on SST from the seasonal perspective. We present the correlation between SST anomalies and SSHA as a measure of influence of subsurface on SST in the TIO (Fig. 3). Influence of subsurface on SST involves not only regional processes but also remote processes such as advective processes. Therefore, the linear in situ correlation coefficient cannot quantify the complete contribution of the subsurface to the SST. Nevertheless, it provides us a simple indicator representing the subsurface influence. The actual contribution may be much higher than that depicted in this analysis. The correlation is significantly high along the Java coast and southwestern Indian Ocean from July to November, coinciding with the observations of X02 (wherein X02 considered all the months for correlation analysis). However, one notable difference is that the high correlation values in the southwestern region lie to the north of the main study area of X02 (shown as box in Fig. 3). Another interesting result from Fig. 3 is that significantly high correlation values are also observed in the NIO, particularly south of India from July to November, which are absent in X02 analysis. During another half of the year, the high correlation along the Sumatra coast and in the NIO is absent. From January to May, the region of high correlation values lies in the region of X02 main study area. It is interesting to note that the interannual variations in the influence of subsurface on SST occurs in regions of shallow seasonal thermocline in the TIO (contours in Fig. 3, D20 < 100m), which confirms that the shallow thermocline is a necessary condition to initiate strong subsurface feedback on SST and thereby air–sea coupling in the TIO.

The above analysis reveals the following important factors. From July to November (i.e. the season when IOD phenomenon is active), the strong subsurface influence on SST takes place in the near-equatorial regions both in the northern as well as the southern TIO. After the demise of the IOD season (from January to May), the strong thermocline feedback confines to the southern TIO. Further, the correlation patterns show a clear east–west orientation in the SIO and a weak orientation in the NIO during all these months. This suggests the influence of latitudinal dependence of long Rossby waves on the influence of subsurface on SST. We also made quantitative estimations of influence of heat fluxes on SST in the regions of strong subsurface influence on SST by correlating NCEP-NCAR re-analysis heat fluxes with SST in the TIO. We found that the influence of heat fluxes on SST is less than the subsurface influence in the regions of strong subsurface influence (not shown).

4. Interannual thermocline variability in the TIO

To emphasize the interannual variability of SSH (a proxy for thermocline depth) in the TIO, we present the first dominant mode of complex EOF in Fig. 4, which accounts for 17% of the interannual variability. The spatial structure of the dominant CEOF mode shows a dipole structure in the SSH fields (Fig. 4a). This structure is observed in several previous studies (Chambers et al., 1999; Feng et al., 2001; Rao et al., 2002a). The major difference from the previous studies is that the present study spans for 50 years while previous longest analyzed record was for 12 years (1982–1998) in Rao et al. (2002a). Although the model used in Rao et al. (2002a) employs forward integration of basic equations using observed winds and heat fluxes, the results from Rao et al. (2002a) are quite similar to the present assimilated fields (compare Fig. 4a with Fig. 3 in Rao et al., 2002a). This suggests that the derived fields from SODA are reliable even for periods other than the TOGA period (1985–1995) of intense observations. The close correspondence is due to the fact that the subsurface dynamics in the TIO is dominantly controlled by ocean–wave dynamics. The clear signature of the Rossby–Kelvin wave pattern seen in Fig. 4a further confirms this. Thus, the phase diagram of first CEOF mode (Fig. 4b) also shows a propagating structure (evident from the increase of phase) from east to west in the off-equatorial regions, a mixture of eastward- and westward propagating signals on the equator, and poleward propagating signals along the eastern boundary. From our basic understanding of tropical dynamics, we infer these propagating signals as off-equatorial Rossby waves, equatorial Kelvin–Rossby waves, and coastal trapped Kelvin waves, respectively.

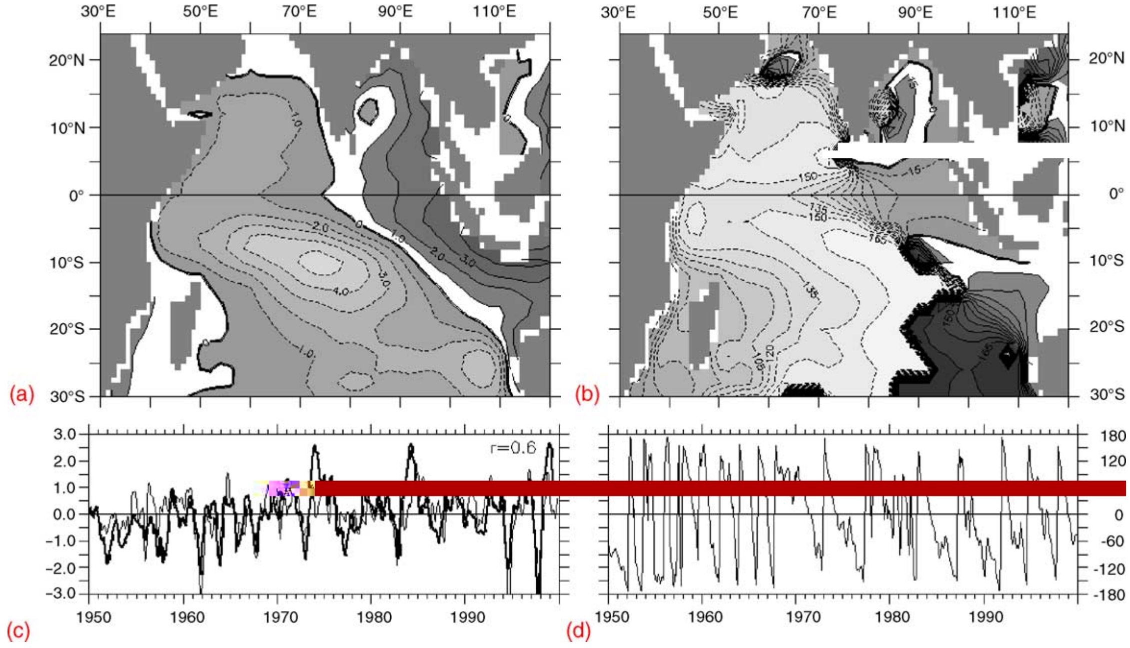

Fig. 4. First leading CEOF mode of SSH anomalies (a) spatial function (real part multiplied by 100) and (b) temporal function (real part divided by 100, bold line). DMI is overlaid (thin line). Temporal function is smoothened by 5 month running mean. Contour interval is 0.1. Dashed (solid) lines denote negative (positive) loadings.

Table 1
Estimated phase speeds of westward propagating waves and theoretical phase speeds of Rossby waves (cm s^{-1})

Latitude	Estimated	Theoretical first mode baroclinic Rossby wave	Theoretical second mode baroclinic Rossby wave
6°S/6°N	−43	−68	−27
8°S	−29	−38	−15
10°S	−20	−24	−10
12°S	−10	−16	−7
14°S	−9	−12	−5

The time series of the amplitude of the first CEOF mode (Fig. 4c) correlates well ($r = 0.6$) with the dipole mode index[2] at zero lag. This clearly indicates that the observed dipole structure in Fig. 4a is closely related to the Indian Ocean Dipole. Another interesting feature in Fig. 4c is the strong seasonal phase locking of the principal component; it shows negative peaks at the end of the year and suddenly changes the phase during the following year. This is also one of the typical features of the Indian Ocean Dipole as explained in Saji et al. (1999) and Rao et al. (2002a). In particular, Rao et al. (2002a) explained the role of long waves in the phase reversal of the surface and subsurface dipole. A spectrum analysis of the leading principal component shows peaks at 2 years and 5 years with a secondary peak at 3 years (not shown), which corresponds to the periodicities of IOD phenomenon (Ashok et al., 2003; Behera and Yamagata, 2003). The principal component of the phase of the first CEOF mode (Fig. 4d) shows gradual propagating signals around those peak periods. Since significant interannual variability in Fig. 4 is confined to the region north of 15°S, we analyze the same area in the present study. One of the objectives of the present study is to find out forces that excite the long waves in the TIO.

5. Interannual Rossby waves in the TIO

5.1. Identification of long waves in the TIO

Time–longitude plots of SSHA for recent years are shown in Fig. 5. At all off-equatorial latitudes, we see clear westward propagation of SSHA with increasing slope towards higher latitudes. These westward propagating signals with decreasing phase speed with increasing latitude are interpreted as Rossby waves. The phase speed of these waves estimated from the time–longitudinal plots of SSHA is tabulated in Table 1 along with the theoretical phase speeds of the first and second baroclinic long Rossby waves (e.g. Philander, 1990), given by

$$C_{\mathrm{R}} = \frac{\beta C^2}{f^2}$$

[2] The dipole mode index is used here instead of Sumatra index to represent the IOD because the former index preserves all seasons as for the Nino index.

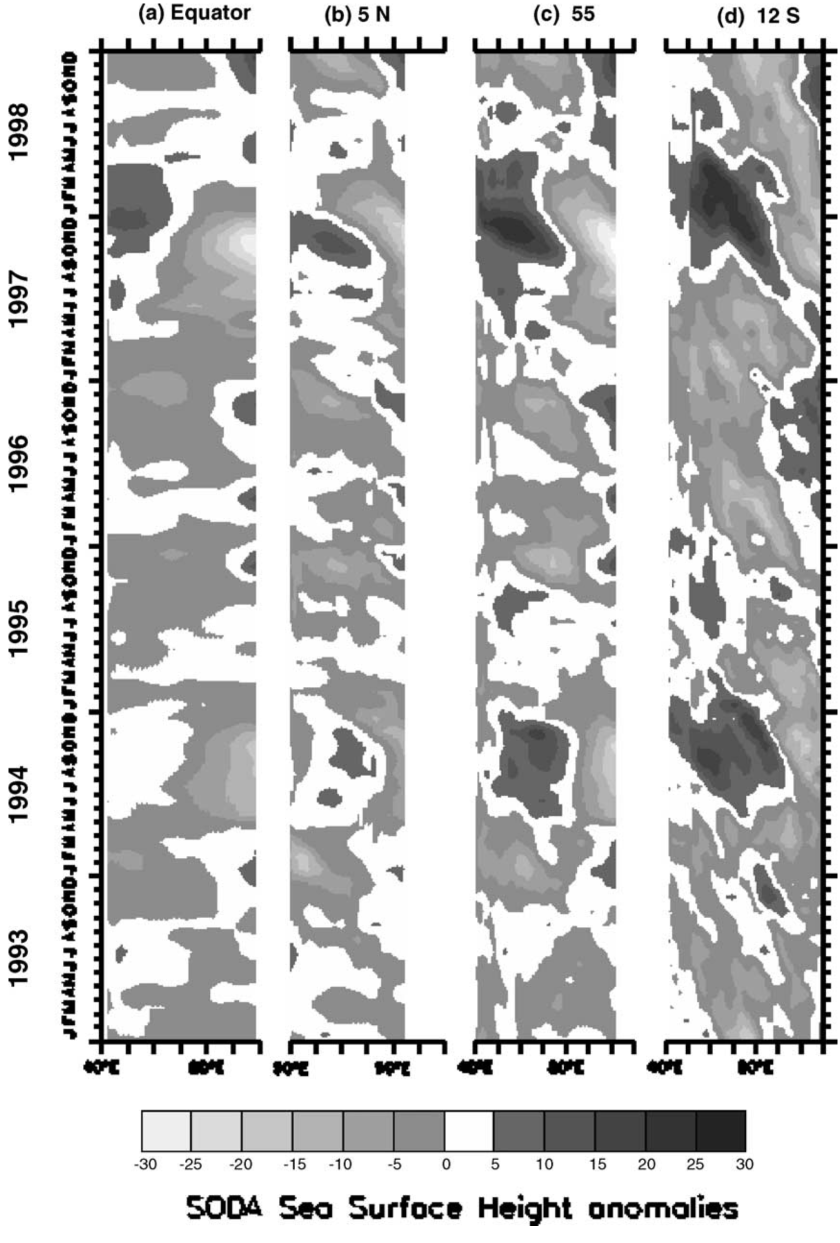

Fig. 5. Time–longitude plots of SODA SSH anomalies (cm) along (a) equator, (b) 5°S, (c) 12°S and (d) 5°N.

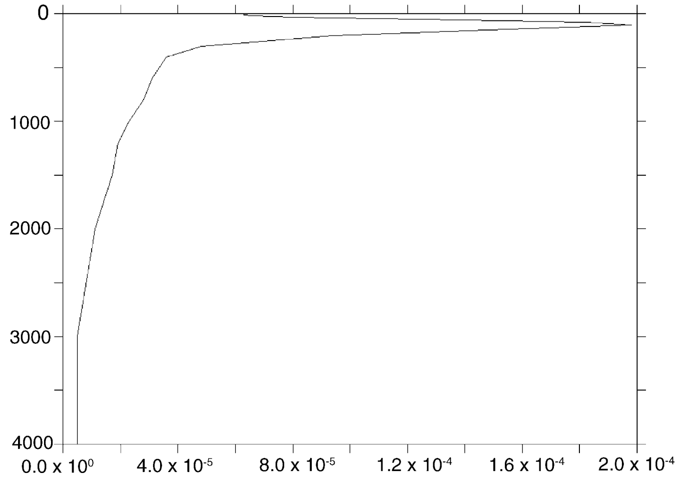

Fig. 6. Typical Brunt–Vaisala frequency profile used in estimating characteristic long wave speeds for different baroclinic modes.

where C_R is the phase speed of Rossby waves, C the long internal gravity wave speed, f the Coriolis parameter, and β is the meridional gradient of f. Characteristic speeds (C) for the first and second baroclinic modes are calculated, following McCreary (1984), as 258 cm s^{-1} and 160 cm s^{-1} based on a typical buoyancy frequency profile in the TIO as shown in Fig. 6. In general, there is a good agreement between measured phase speeds and the theoretical ones. Although the measured phase speeds are smaller compared to the theoretical ones, the decrease with increase in latitude is clearly simulated. The measured values are between the first and second baroclinic Rossby wave speeds. Chambers et al. (1999) and Rao et al. (2002a) also estimated the phase speed from Topex/Poseidon and model outputs and found that the estimated value is less compared to the theoretical value of the first baroclinic mode Rossby wave. They conclude that it is due to the combination of first and second baroclinic modes in the observed wave propagation (see also Aiki and Yamagata, 2000). Note that the estimated Rossby wave speeds in this article are slightly different from those in Rao et al. (2002a) because of different methodologies and datasets used. It may be noted that space–time structure of the wind forcing can also affect the apparent westward propagation speeds. In the following, we discuss how these Rossby waves are forced and how they are associated with the known interannual signals in the tropics.

5.2. *Forcing mechanisms of the Rossby waves*

Physical processes that govern the large-scale, low-frequency variations in the off-equatorial thermocline are largely related to Ekman pumping, variation of thermocline depth at the eastern boundary, and Rossby wave propagation (Meyers, 1979). From previous studies (Perigaud and Delecluse, 1992, 1993; Masumoto and Meyers, 1998), it is evident that the contribution of local Ekman pumping alone cannot explain the thermocline changes very well. This fact is also verified in the present study by looking at the correlation between local Ekman pumping velocity and SSHA; the correlation coefficient is insignificant (<0.2) in many regions except for the region near Sumatra (not shown). Therefore, it is essential to look at the thermocline variability through Rossby waves; the Rossby waves can be forced either by wind stress curl over the interior TIO and/or by thermocline variations at the eastern boundary of the basin. A simple reduced-gravity model governing the vertical displacement of thermocline depth (or layer interface) is

$$h_t + C_R h_x = W,$$

where W is the Ekman pumping velocity, C_R the non-dispersive long Rossby wave speed at a given latitude, t the time, and x is the distance from the eastern boundary (cf. Meyers, 1979).

We carry out two experiments to determine the exact forcing of the thermocline variability in the TIO. In the first set of experiment, variations at the eastern boundary are kept zero. Therefore, the thermocline variability through Rossby waves along a particular latitudinal belt is caused mainly due to Ekman pumping in the interior TIO. In the second experiment, the variations at the eastern boundary are prescribed from the SODA dataset. These experiments are carried at different latitudinal belts and results for 6°N and 10°S are shown in Fig. 7. Results for other off-equatorial latitudinal belts in between also reveal the similar results (not shown). Since the interior thermocline variability is well captured by first set of experiments (Fig. 7a), it is concluded that the dominant portion of the thermocline interannual variability in the interior TIO is forced by the Ekman pumping integrated along the characteristic line of Rossby waves (Fig. 7a and c). By including variations at the eastern boundary in the first set of experiment, it is found that eastern boundary variations are important only near the eastern boundary and its influence is relatively small in the interior TIO (Fig. 7b).

The wind stress curl that is responsible for generating Rossby wave is primarily concentrated in particular regions rather than along the whole path as evident in Fig. 8. We have found two active regions of wind stress curl in the southern TIO from the composite analysis discussed in Section 5.3 (see also Fig. 11a); one is the region surrounded by the box (80°E–90°E, 15°S–5°S), and another is located further southeast in the region surrounded by the box (90°E–100°E, 20°S–10°S). We have correlated the wind stress curl anomalies, averaged from September to November for the northern region and from October to December for the southeastern region (coinciding with the evolution of these anomalies; see Fig. 11a), with SSHA at different latitudes to check the influence of this forcing on SSH. It is clear from Fig. 8 that the wind stress curl at these particular regions generates the observed Rossby wave signals in the interior Indian Ocean. The SSH correlation with the wind stress curl anomalies in both the regions shows a westward propagating feature at all latitudes between 2°S and 16°S. The correlation with wind stress curl anomalies is stronger in the northern region at all latitudes prior to December (indicated as bold line in Fig. 8), while the correlation is strong in the southern region after December only between 14°S and 16°S latitudinal belt. We note that the wind stress curl anomalies in the northern region are strongly correlated with the Sumatra index ($r = 0.7$), while those in the southeastern region are equally highly correlated with ENSO index

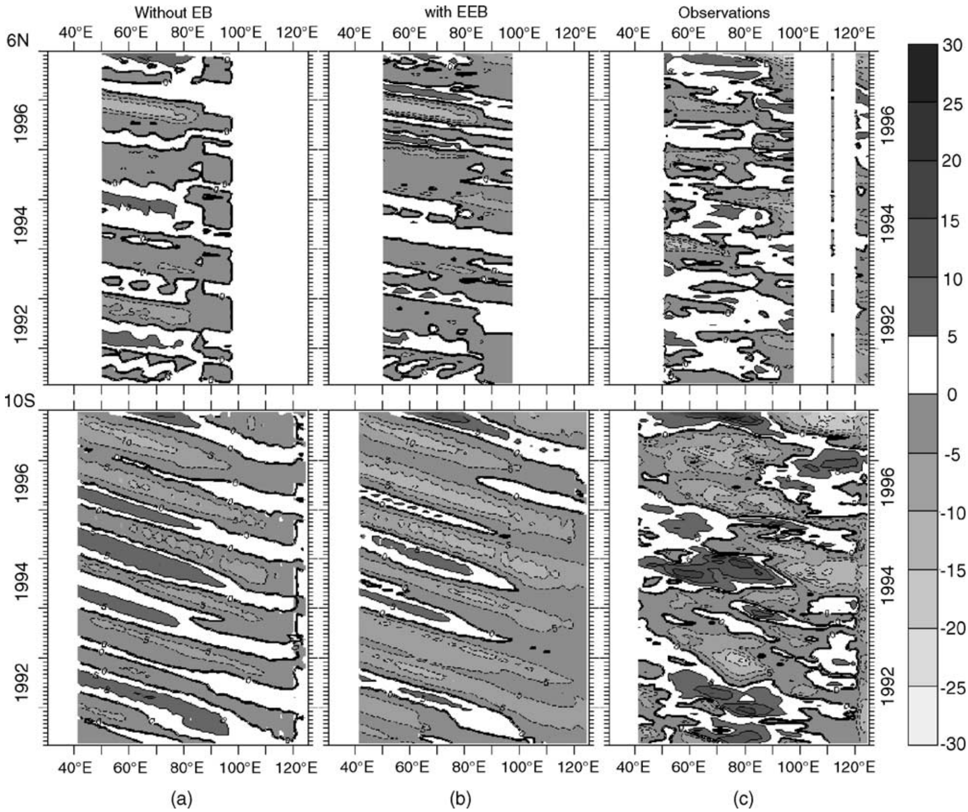

Fig. 7. Simulated D20 anomaly along 10°S: (a) the eastern boundary conditions are assumed zero throughout the integration, (b) with the eastern boundary conditions considered, (c) observed D20 anomaly.

($r = 0.7$). We also carried out similar analysis using the wind stress curl in the NIO (at the northern tip of Sumatra) and found similar propagating signals between 2°N and 8°N (not shown).

5.3. Relation between interannual Rossby waves and climate variations

Fig. 9a shows the correlation coefficients of SSHA at different latitude belts with the Sumatra and ENSO indices. Signs of the correlation coefficients with the Sumatra index are reversed for convenience of comparison. Significant positive correlation patterns show clear westward propagating signals with the Sumatra index at all latitudes both in NIO and SIO. However, the positive correlation patterns with the ENSO index show such westward propagating signals only in the SIO. We also note weakening of the correlation with the Sumatra index from the near-equatorial to higher latitude region whereas strengthening of the correlation with the ENSO index from equatorial regions to higher latitude. Another interesting point is that the correlation associated with the ENSO index becomes higher in the following January after the demise of the IOD (indicated by bold lines in Fig. 9a).

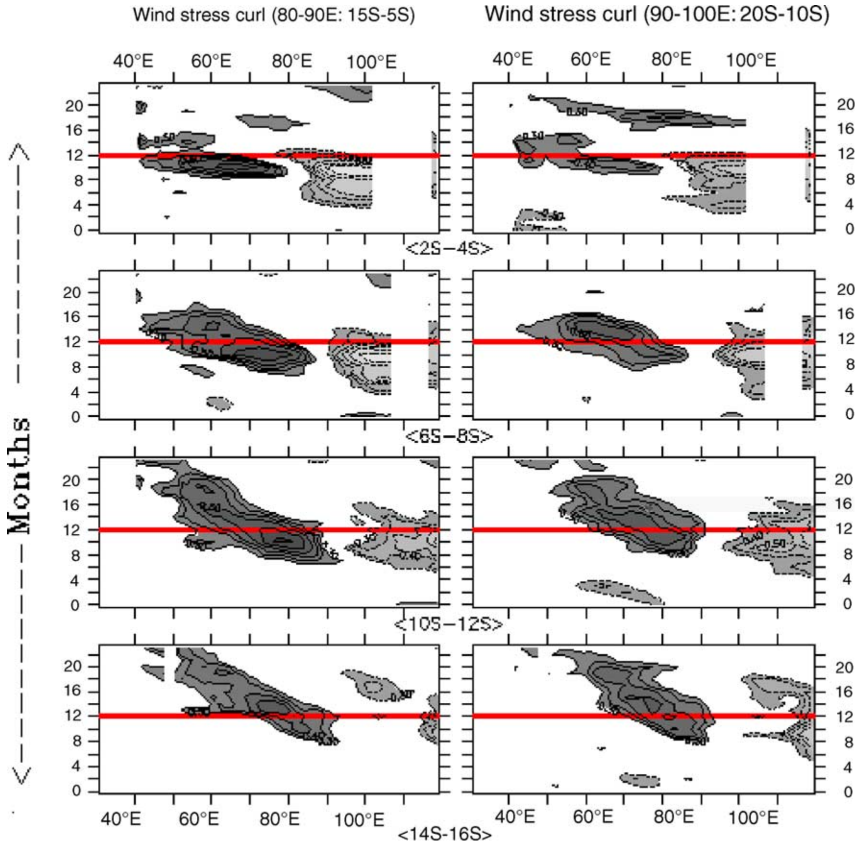

Fig. 8. Correlation between SSH anomalies and wind stress curl anomalies in the region 80°E–90°E; 15°S–5°S averaged for September–November (left) and wind stress curl anomalies in the region 90°E–100°E; 10°S–20°S averaged from October to December (right) at different latitude belts. In this plot and following correlation plots, the first contour is 0.3/−0.3 and contour interval is 0.1.

However, in general, the correlation with the Sumatra index is higher at all latitudes during their inception. The dominance of the Sumatra index over the ENSO index is clearly seen during the IOD season from July to December. All the above observations lead to a conclusion that the observed interannual Rossby waves in the TIO are strongly associated with the IOD especially north of 10°S. ENSO phenomenon, however, dominantly controls the intensification of Rossby wave signals south of 10°S after the demise of the IOD. These results are much more prominent, if we use original DMI and Nino3 indices to represent Indian Ocean and Pacific Ocean interannual coupled phenomenon, respectively. Fig. 9b shows the partial correlation of SSHA with DMI and Nino3 along different latitudinal belts in the TIO. The dominance of Indian Ocean coupled phenomenon north of 10°S is clearly evident, while ENSO dominance in this region is almost insignificant. However, ENSO dominance on the subsurface south of 10°S is also clearly evident from this figure.

Having identified that the interannual Rossby waves north of 10°S are primarily associated with the IOD phenomenon, we further pursue the forcing due to IOD and ENSO here. It is already evident in Section 5.2 that the main forcing for the interannual Rossby waves is due to Ekman pumping induced by wind stress curl in the interior

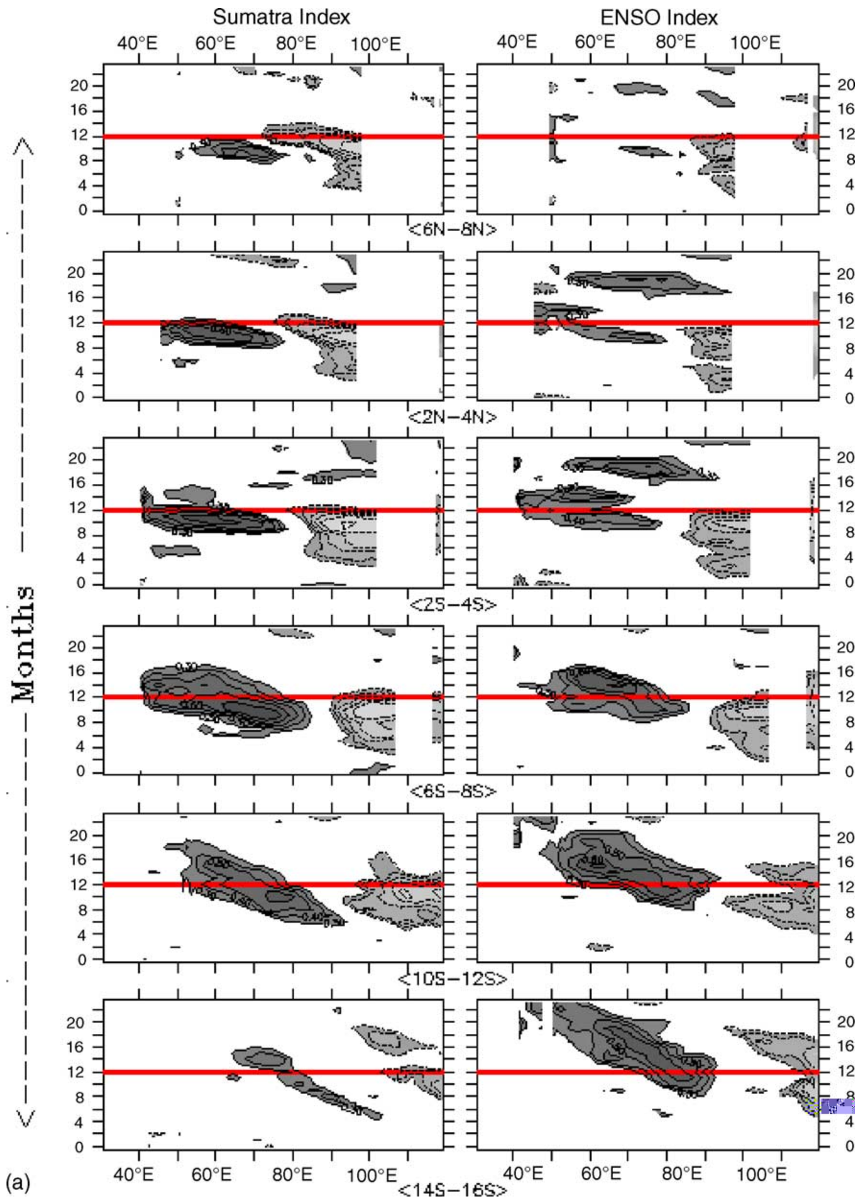

Fig. 9. (a) Same as Fig. 6 but for left (Sumatra index) and right (ENSO index); (b) same as (a) but partial correlations for left (dipole mode index) and right (Nino3 index).

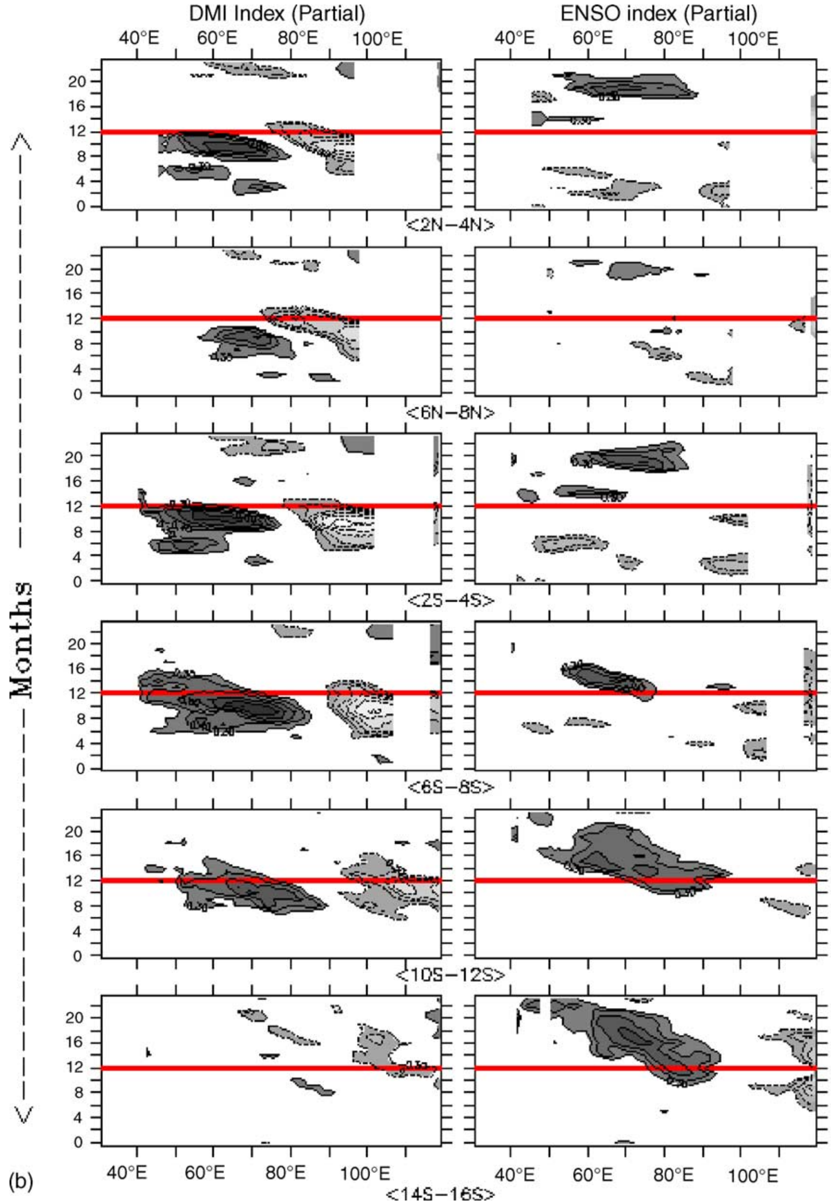

Fig. 9. (*Continued*).

TIO. Therefore, it is of interest to check how the wind stress curl anomalies are related to the two dominant interannual climate signals of the ENSO and the IOD. Fig. 10a shows the correlation coefficient with the Sumatra and ENSO indices. The correlation with the Sumatra index continuously evolves from July and becomes remarkable in September and

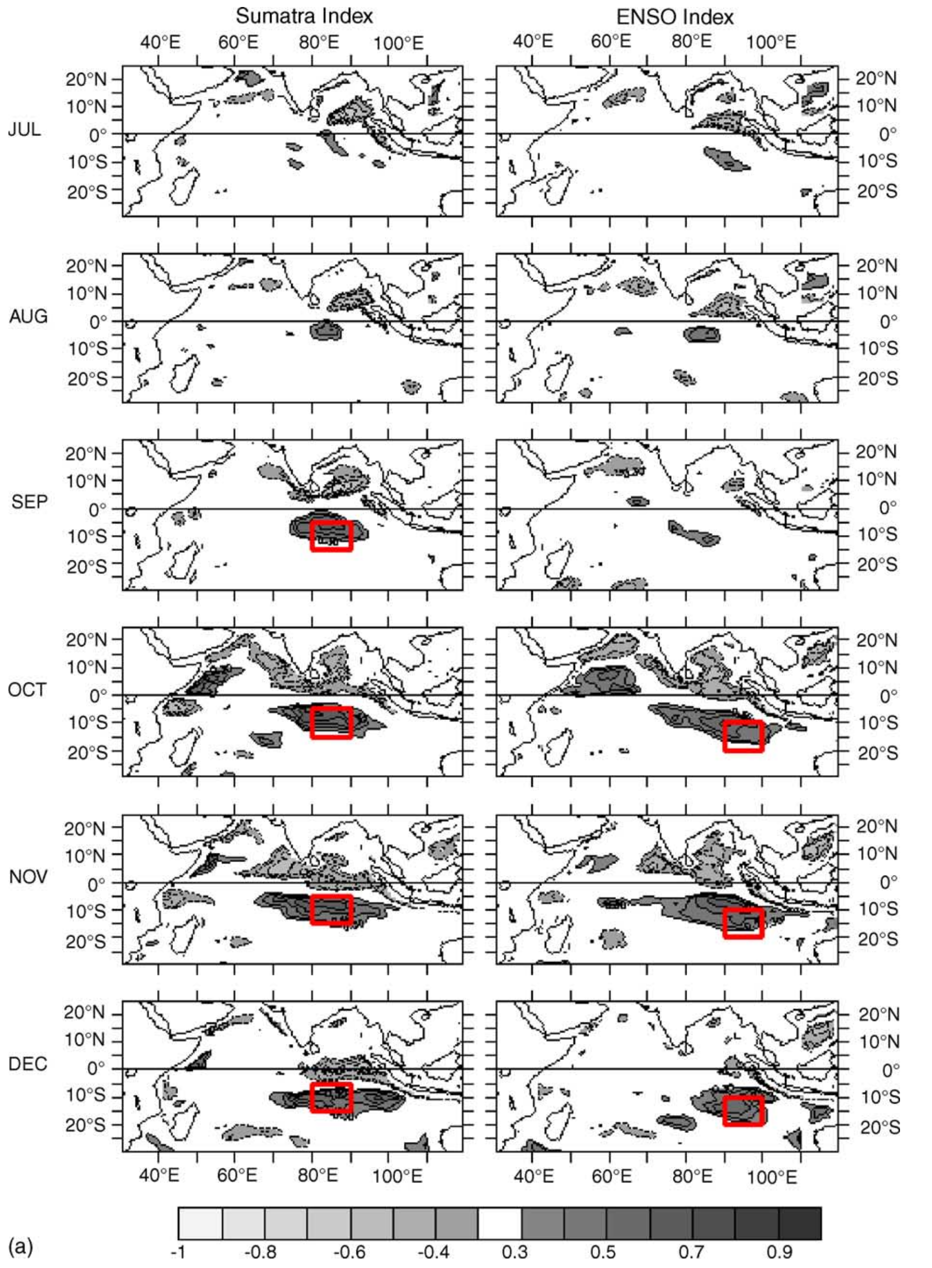

Fig. 10. (a) Correlation between wind stress curl anomalies and Sumatra index (left) and ENSO index (right); (b) same as (a) but for partial correlation. *Left*: Sumatra index with linear response of ENSO index removed. *Right*: ENSO index with linear response of Sumatra index removed.

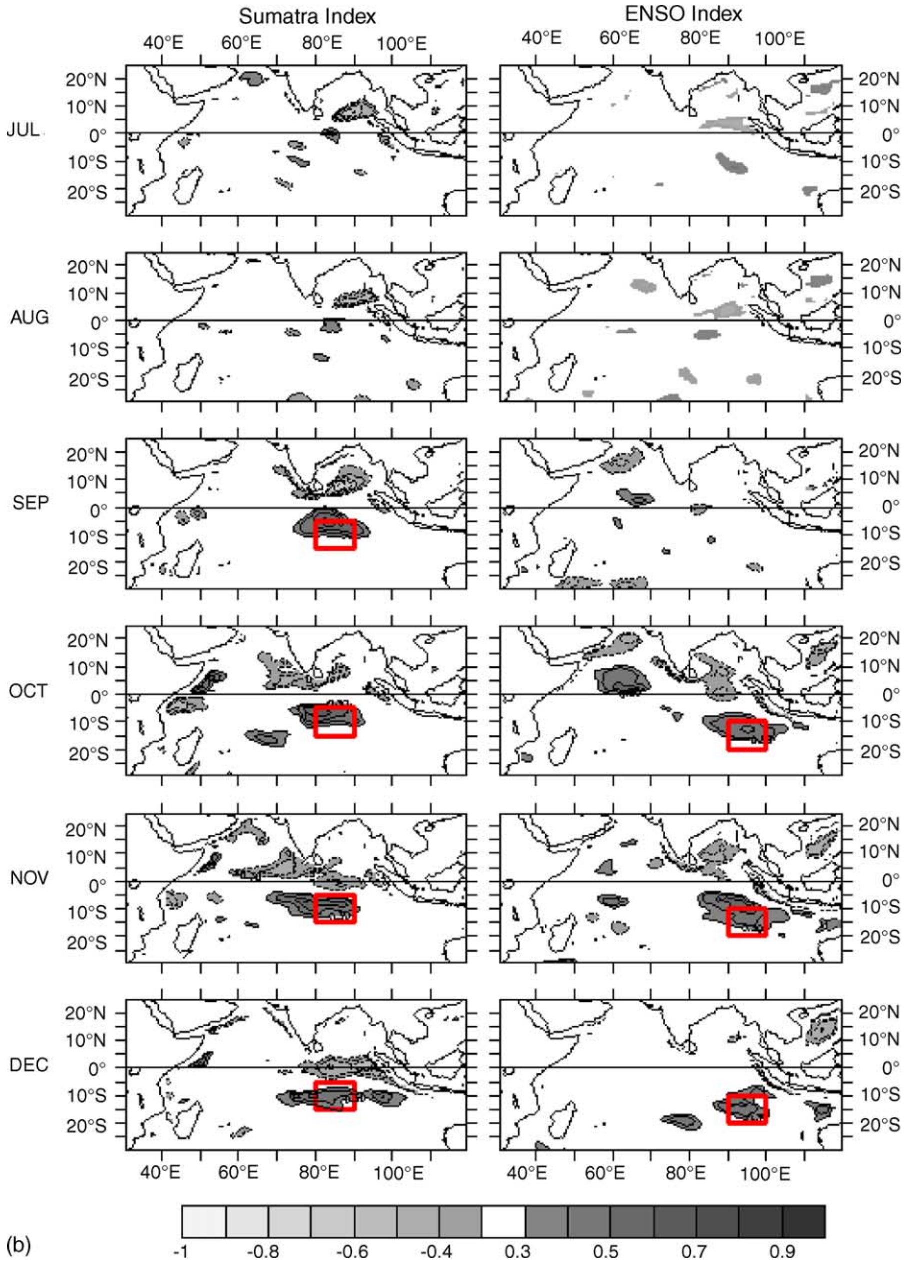

Fig. 10. (*Continued*).

lasts till December. Surprisingly, the correlation pattern with the ENSO index is similar to the correlation pattern with the Sumatra index except that the former is weaker and not significant in September. Another interesting point is that the negative correlation with the Sumatra index in the NIO seems to propagate to the west, while positive correlation in SIO seems to be stationary. Interestingly, no such propagation is observed with the ENSO index in NIO. The significant correlation with the ENSO index in SIO seems to be stationary.

Since 35% of the IOD events co-occurred with the ENSO events (Rao et al., 2002a; Yamagata et al., 2002, 2003), it is possible that the observed correlations in Fig. 10 may be due to overlapping of these two signals during certain years. To make a meaningful interpretation of the correlation pattern observed in Fig. 10a, we calculated partial correlations by removing the linear contribution of ENSO (Sumatra) index from correlation with the Sumatra (ENSO) index. No significant changes in the correlation pattern with the Sumatra index are observed after removing the linear response due to the ENSO index (Fig. 10b), except that the correlation coefficients are slightly reduced by 0.1 after October. On the other hand, the correlation with the ENSO index shows significant differences after removing the linear response of the Sumatra index. For example, the high correlation region shrinks in SIO after October with weakening of correlation. This analysis demarcates the regions of significant correlation particularly in the SIO (compare Fig. 10a and b). This shows that the observed correlation with the ENSO index is mainly due to the co-occurrence of ENSO and IOD events in some years. Since significant correlation coefficients are still seen from October to December, it may be possible for these two climate signals to interact during some years.

We also prepared composite maps of wind stress and curl anomalies (Fig. 11a) and SSHA (Fig. 11b) for pure positive IOD (positive IOD events occurred without warm ENSO events; 1953, 1961, 1967, 1977, and 1994) and pure warm ENSO events (warm ENSO events occurred without positive IOD events; 1965, 1969, 1976, 1986, and 1991) to strengthen the above claim. Fig. 11a shows the wind stress and curl anomalies composite of five such pure events during the study period. Owing to the anomalous easterlies at the equator and anomalous northwesterlies in the eastern SIO, strong anti-cyclonic anomalies are observed on either side of the equator during pure IOD events until November/December in the eastern TIO. Such a circulation pattern is reminiscent of the Matsuno–Gill type pattern. The ENSO composite does not show any such consistent and organized pattern of wind stress curl anomalies; the wind stress anomalies associated with the ENSO are weaker (Fig. 11a) as shown by Rao et al. (2002a). However, strong consistent anti-cyclonic anomalies are observed in the SIO around 20°S from July to the following May. Fig. 11b shows SSHA composite for pure IOD and pure ENSO events. In agreement with wind changes, strong positive anomalies in SSH are observed in the IOD composite both in NIO and SIO, particularly north of 12°S in the TIO. In contrast, the pure ENSO composite shows the stronger positive anomalies south of 10°S from the following January, which correspond to the strong anomalous anti-cyclonic curl in this region (Fig. 11a). Considering these meridional differences in IOD versus ENSO composites of SSHA and meridional differences in the thermocline feedback (Fig. 3), we refer to the positive SSH anomalies in the region north of 10°S as the northern flank of SIO ridge (2°S–10°S) and those in the region south of this latitude as the southern flank of the SIO ridge (10°S–16°S) (indicated by boxes in Fig. 11b)

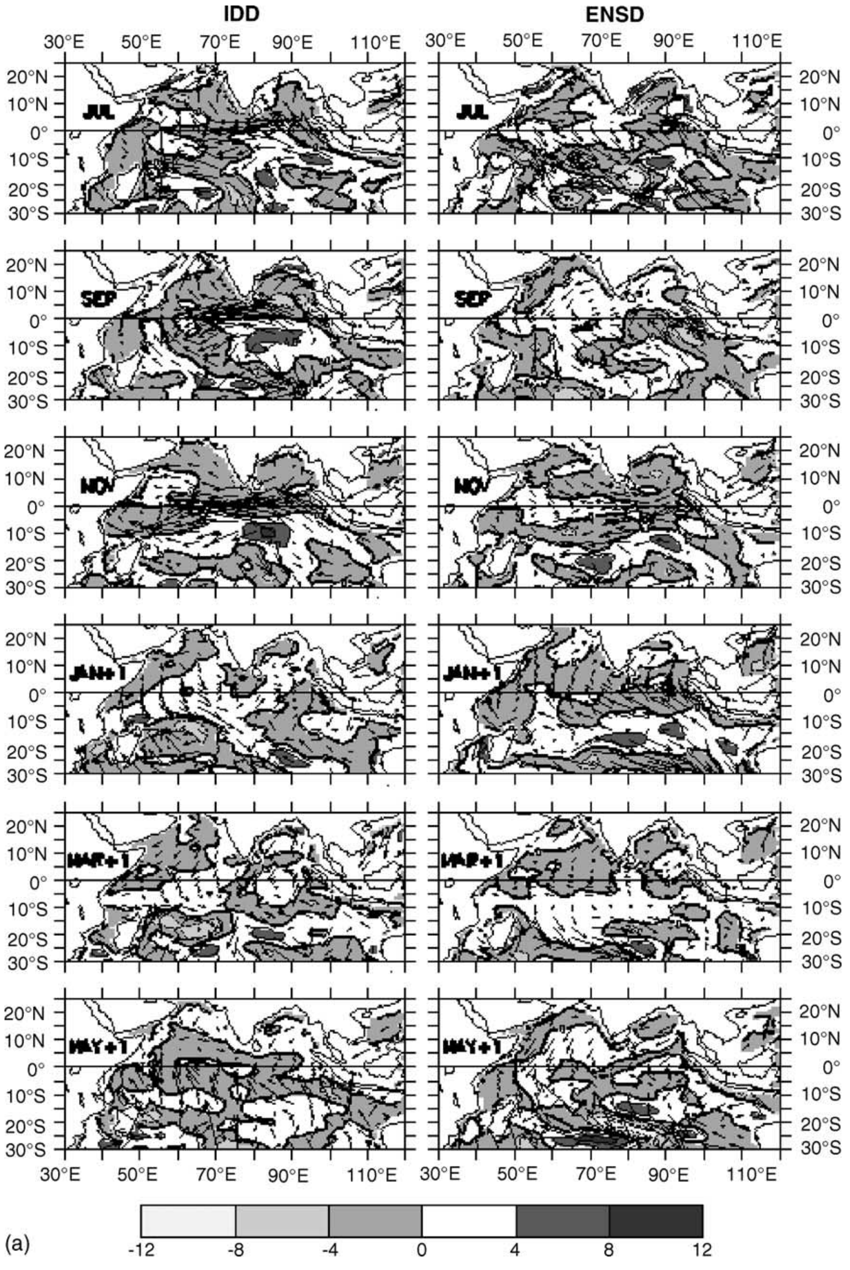

Fig. 11. (a) Composite of wind stress curl anomalies for pure IOD (left) and pure ENSO (right) events. Wind stress vectors are overlaid. (b) Same as (a) but for SSH anomalies.

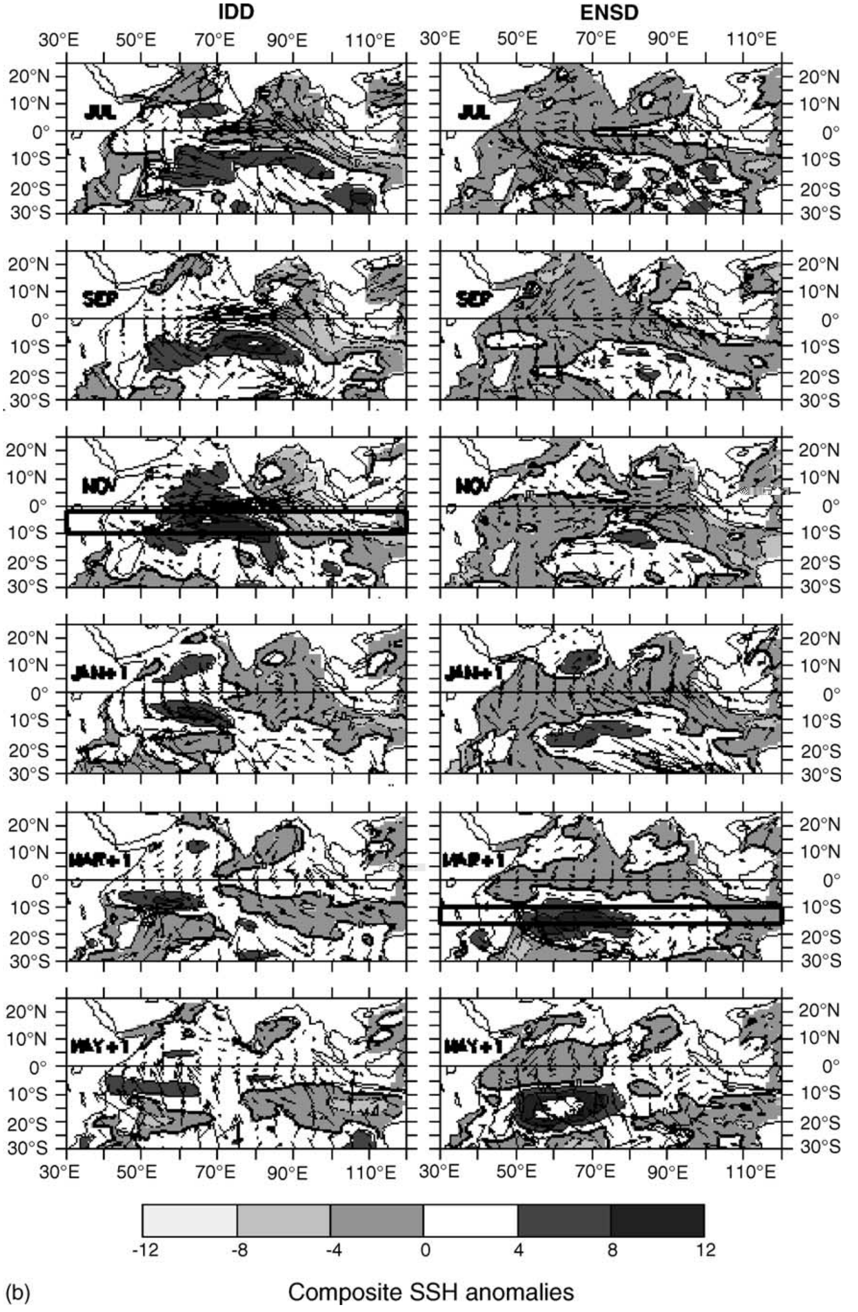

Fig. 11. (*Continued*).

in the following discussions. We also note that time evolution of these anomalies is quite different for these two ridges. It is obvious from the previous discussion that variations in the northern ridge are mostly associated with the IOD, while variations in the southern flank are mainly associated with the ENSO.

From the above discussion, we conclude that interannual Rossby waves in the TIO are initiated by the IOD related anomalous wind stress curl and also strengthened by these winds till the demise of the IOD phenomenon by December. At higher latitudes, south of 10°S, ENSO-related winds significantly strengthen the Rossby waves after November/ December.

6. East African rainfall and the subsurface influence on SST in the TIO

X02 showed that the variability in the thermocline ridge in the southwestern Indian Ocean has a significant influence on the number of cyclones that form in the vicinity of this ridge. Since the thermocline ridge migrates southward from boreal summer to winter, it is interesting to find out the variations in teleconnection pattern associated with the migration of the thermocline ridge from north to south with seasons. Here, we focus on the northern flank of the SIO ridge. Fig. 12a shows the correlation of rainfall anomalies for September–November with the northern flank of the SIO ridge and also with the Sumatra index. The teleconnection patterns related with the northern flank during the boreal fall are similar to those obtained with the Sumatra index (Fig. 12a and b). Saji and Yamagata (2003b) derived the IOD-related teleconnection patterns and distinguished those from ENSO-related teleconnection patterns. The teleconnection patterns observed with the Sumatra index as well as with the northern flank of the SIO ridge are clearly seen in Saji and Yamagata

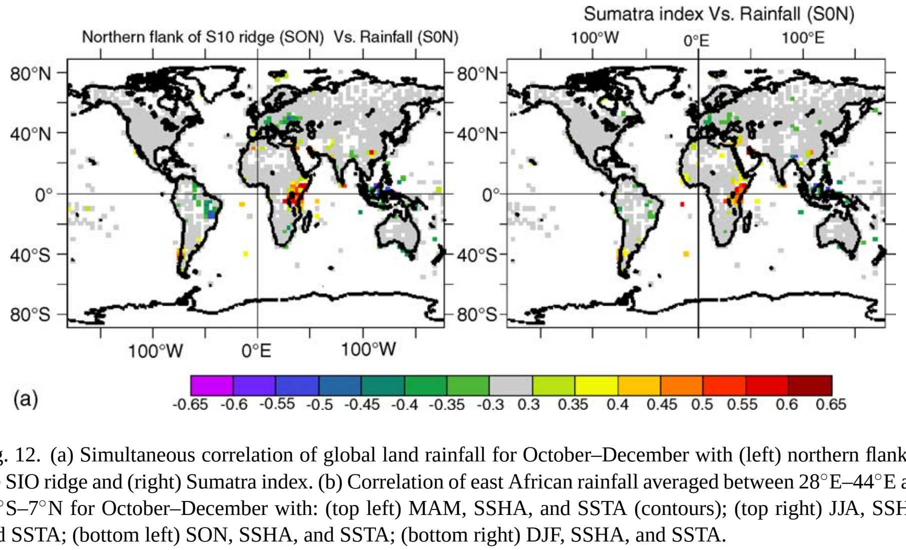

Fig. 12. (a) Simultaneous correlation of global land rainfall for October–December with (left) northern flank of the SIO ridge and (right) Sumatra index. (b) Correlation of east African rainfall averaged between 28°E–44°E and 10°S–7°N for October–December with: (top left) MAM, SSHA, and SSTA (contours); (top right) JJA, SSHA, and SSTA; (bottom left) SON, SSHA, and SSTA; (bottom right) DJF, SSHA, and SSTA.

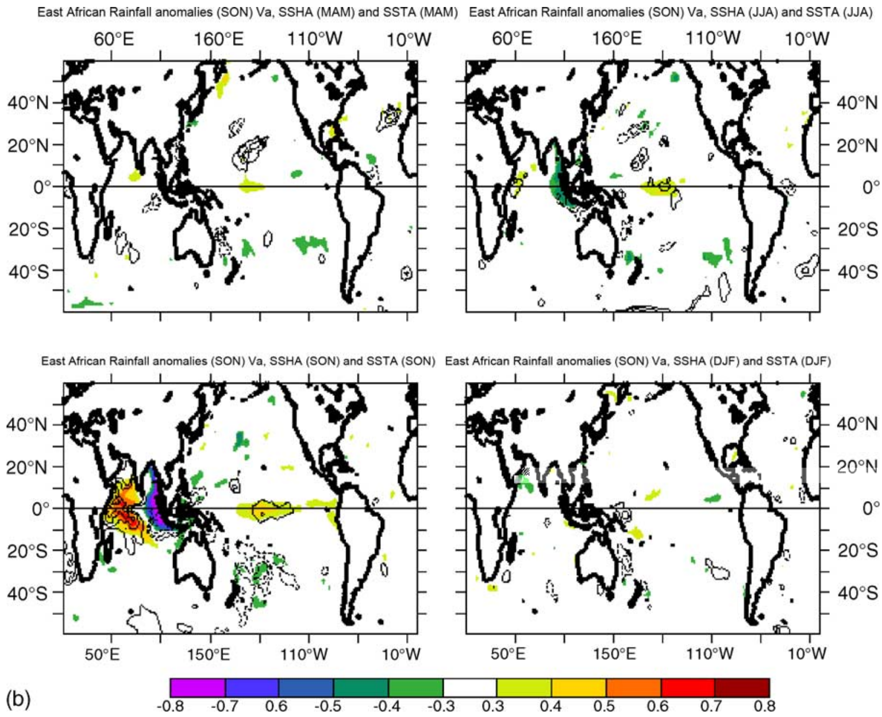

(b)

Fig. 12. (*Continued*).

(2003b). This suggests that the observed teleconnection patterns are in fact related to the IOD.

The most important feature in Fig. 12a is higher correlation coefficients (>0.5) over the central eastern Africa with the northern flank of SIO ridge during the boreal fall (Fig. 13).

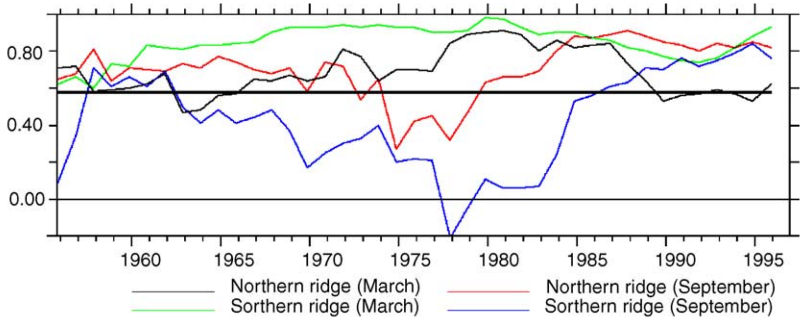

Fig. 13. Running correlation (11 year) between SSH anomalies in the northern flank of the SIO ridge and SST anomalies in the same region (black) during March and (red) during September. Running 11 year correlation between southern flank of the SIO ridge SSH anomalies and SST anomalies during March (green) and September (blue).

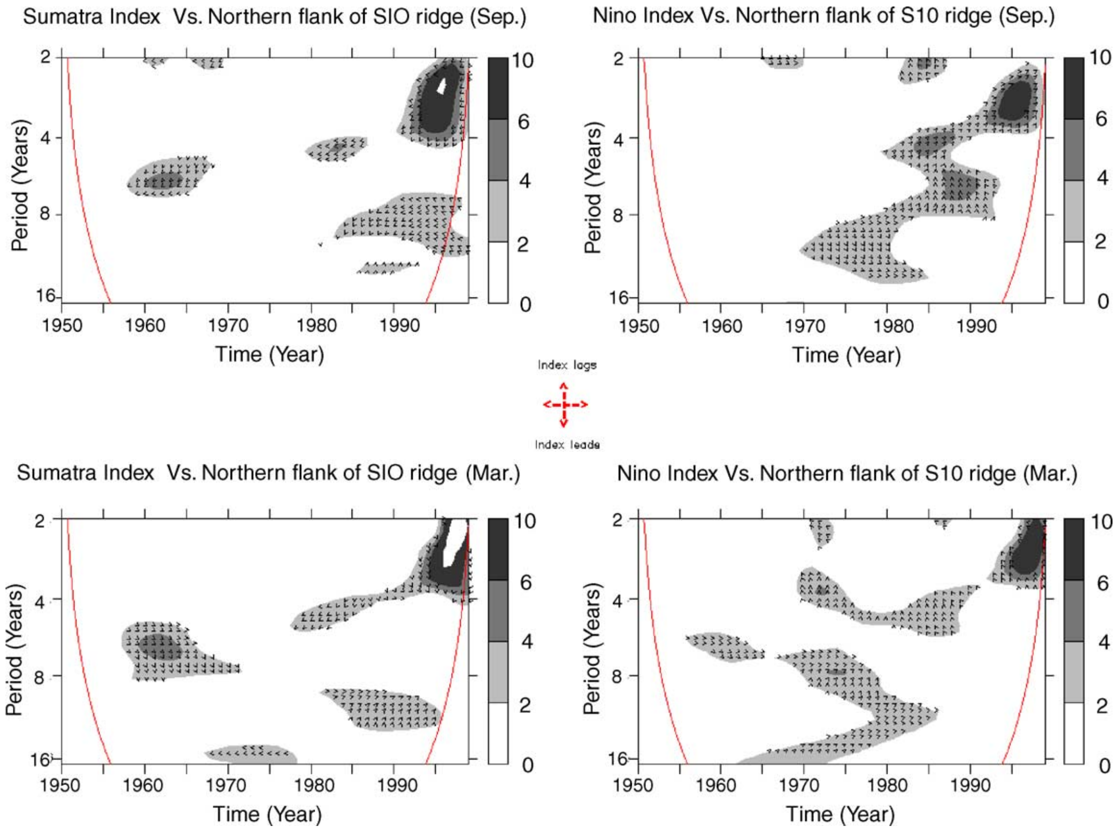

Fig. 14. Cross-wavelet spectrum between Sumatra index and northern flank of the SIO ridge for September (top left), ENSO index and northern flank (top right), Sumatra index and southern flank (bottom left), and ENSO index and southern flank during March. Vectors show the phase (bottom right). Regions with above 95% confidence limit are only plotted.

It is interesting to study whether this ridge holds any predictive capability for the African rainfall. To check this, we have correlated the east African rainfall averaged in the region (28°E–44°E; 10°S–7°N) for October–December (referred to as short rains) with the global SSHA at different lag and lead times. A significantly high correlation is found along the eastern Indian Ocean by one season (June–August) prior to the short rains. The correlation pattern is reminiscent of the coastal trapped anomalous upwelling Kelvin wave along Sumatra, Java, and the eastern Bay of Bengal. Ocean dynamics related to IOD (Vinayachandran et al., 1999; Murtugudde et al., 2000; Rao et al., 2002a) suggests that this Kelvin wave is due to the anomalous equatorial easterly wind anomalies. Associated with the equatorial upwelling and strong anomalous anti-cyclonic curl in the off-equatorial regions, downwelling Rossby waves are excited and propagated to the west. These Rossby waves are seen in the correlation pattern in the western Indian Ocean during September–November season. The SSHA in the NIO also significantly correlates with the east African short rains,

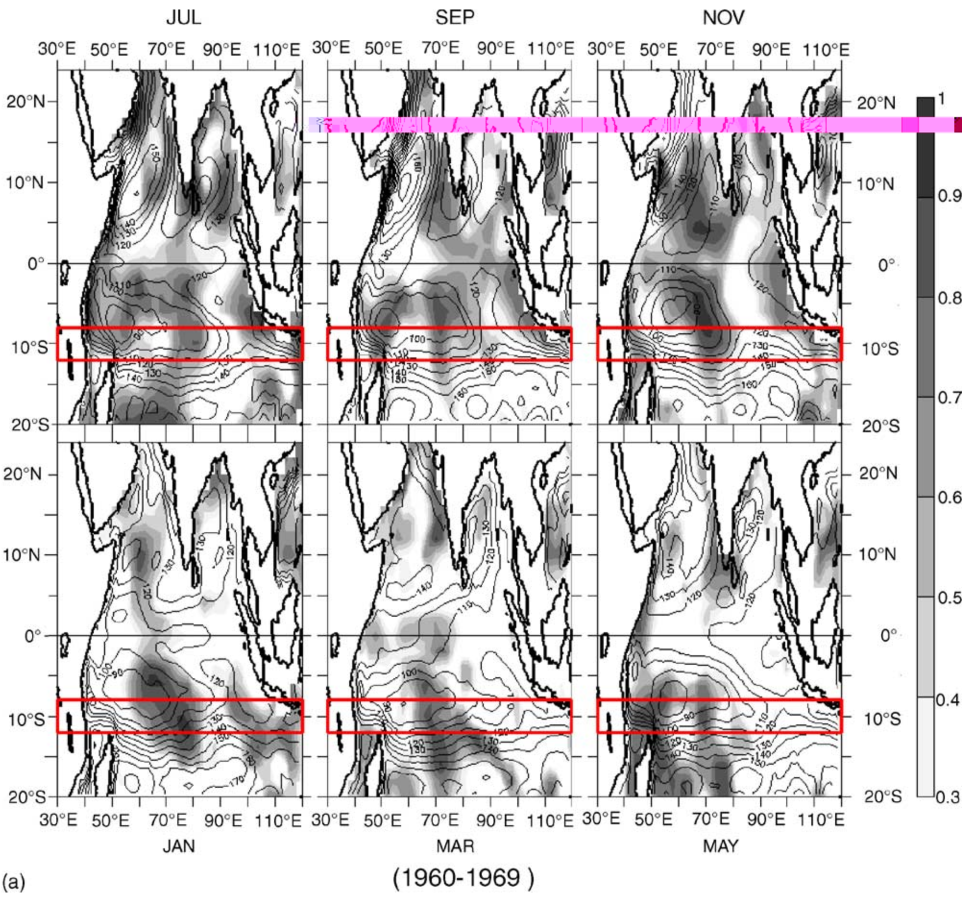

Fig. 15. Same as Fig. 3 but for (a) 1960–1969; (b) 1970–1979; (c) 1980–1995.

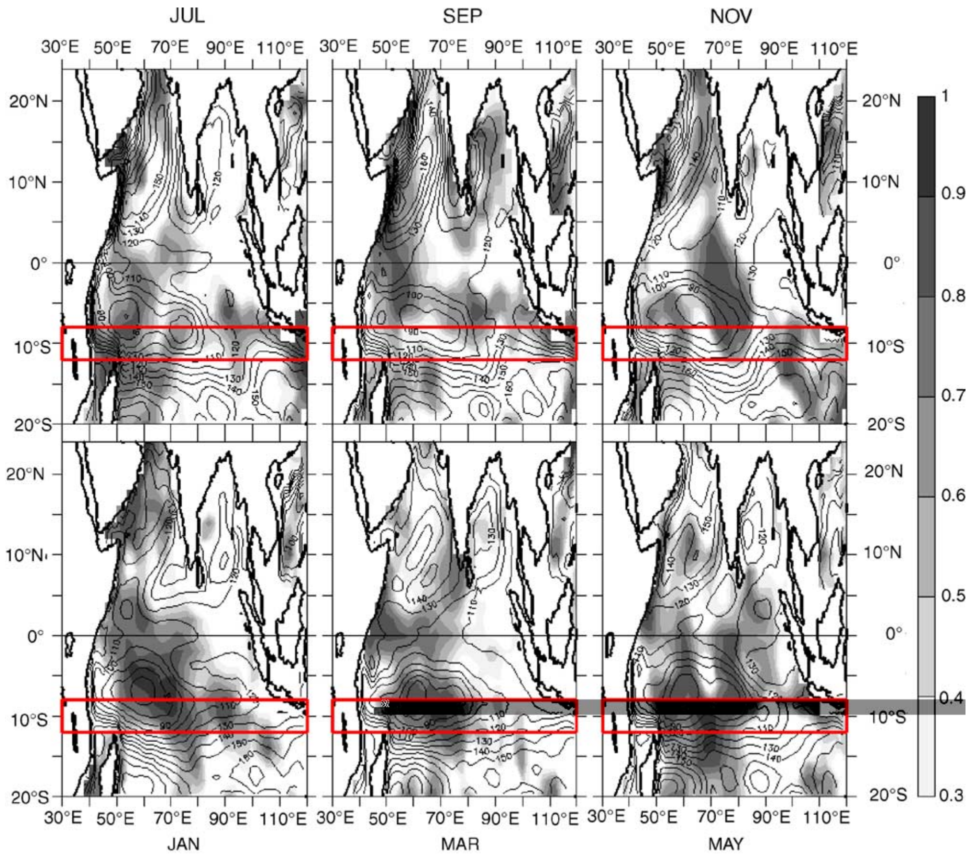

(b) (1970 - 1979)

Fig. 15. (*Continued*).

confirming that during this season, both NIO and SIO are important contributors for the thermocline feedback. This shows that the propagating thermocline ridge in the interior TIO associated with the IOD (farther off the eastern Africa) holds considerable predictable capability for the prediction of the central east African rainfall. The wane of significant correlations during December–February corresponds to the demise of IOD phenomenon in the TIO.

Previous studies (Saji et al., 1999; Latif et al., 1999; Birkett et al., 1999; Behera et al., 1999; Saji and Yamagata, 2003b) have already noticed this link between (boreal fall/winter) east African rainfall with the western Indian Ocean SSTs. What we have shown here is that these SSTs responsible for the east African rainfall are resulted from the strong subsurface influence due to the propagating Rossby waves related to the IOD events. This fact can be verified by looking at the correlation with SSTA and SSHA together. At all places where significant correlations with SSHA are observed, we also observe significant correlation with SSTA (shown as contours in Fig. 12) as well. One region of exception for

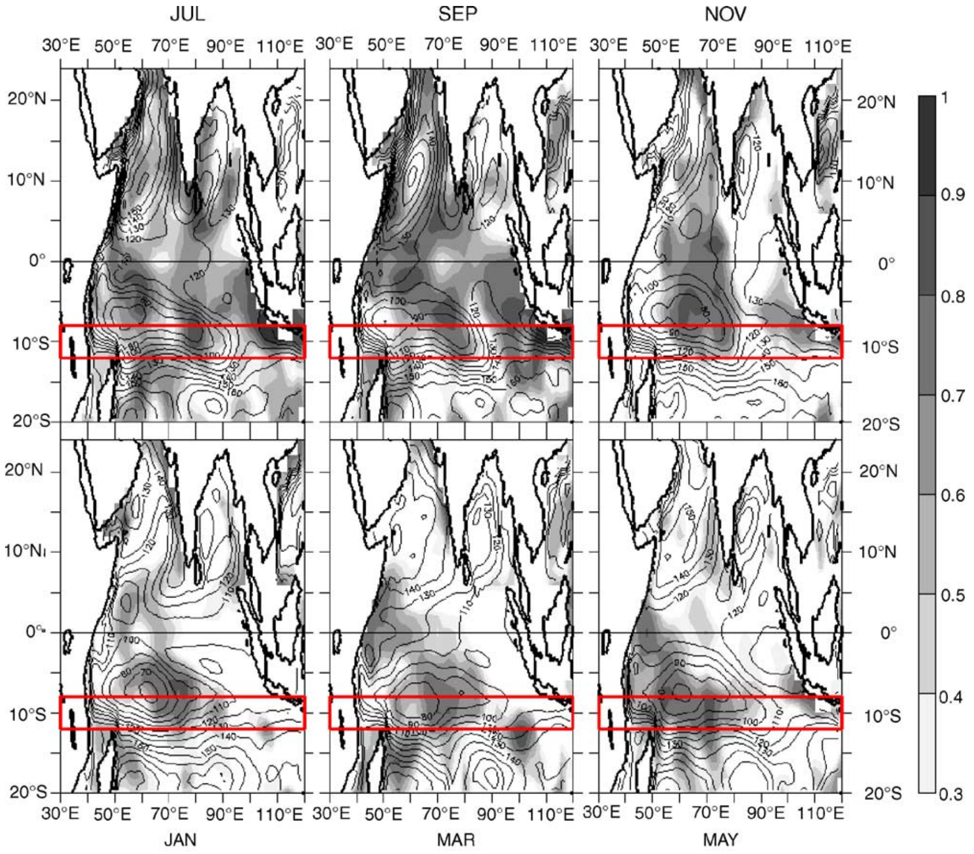

(c) (1980 - 1995)

Fig. 15. (*Continued*).

this coupling is the Bay of Bengal. Here, we do not see any significant correlation with SSTA despite the strong correlation with SSHA. This is because of the strong near-surface stratification in the Bay of Bengal, which inhibits the coupling between subsurface ocean processes and SSTA (Rao et al., 2002b). Further, we note in Fig. 12b that the SSHA shows higher correlations extended to large regions compared to correlation with SSTA. The multiple regression analysis of the east African short rains using both SSTA and SSHA gives better estimate of r (0.5) at a lead time of one season. This suggests that the subsurface influence cannot be ignored for developing reliable prediction schemes for the east African short rains. It is interesting to note that there is little organized correlation in the Pacific, indicating that rainfall anomalies in this region are not related so much to the ENSO.

The probable scenario involved in enhancing the east African rainfall is as follows. The arrival of a downwelling Rossby wave into the western Indian Ocean during IOD events significantly enhances the SSTs in the western Indian Ocean (see Fig. 3). The enhanced

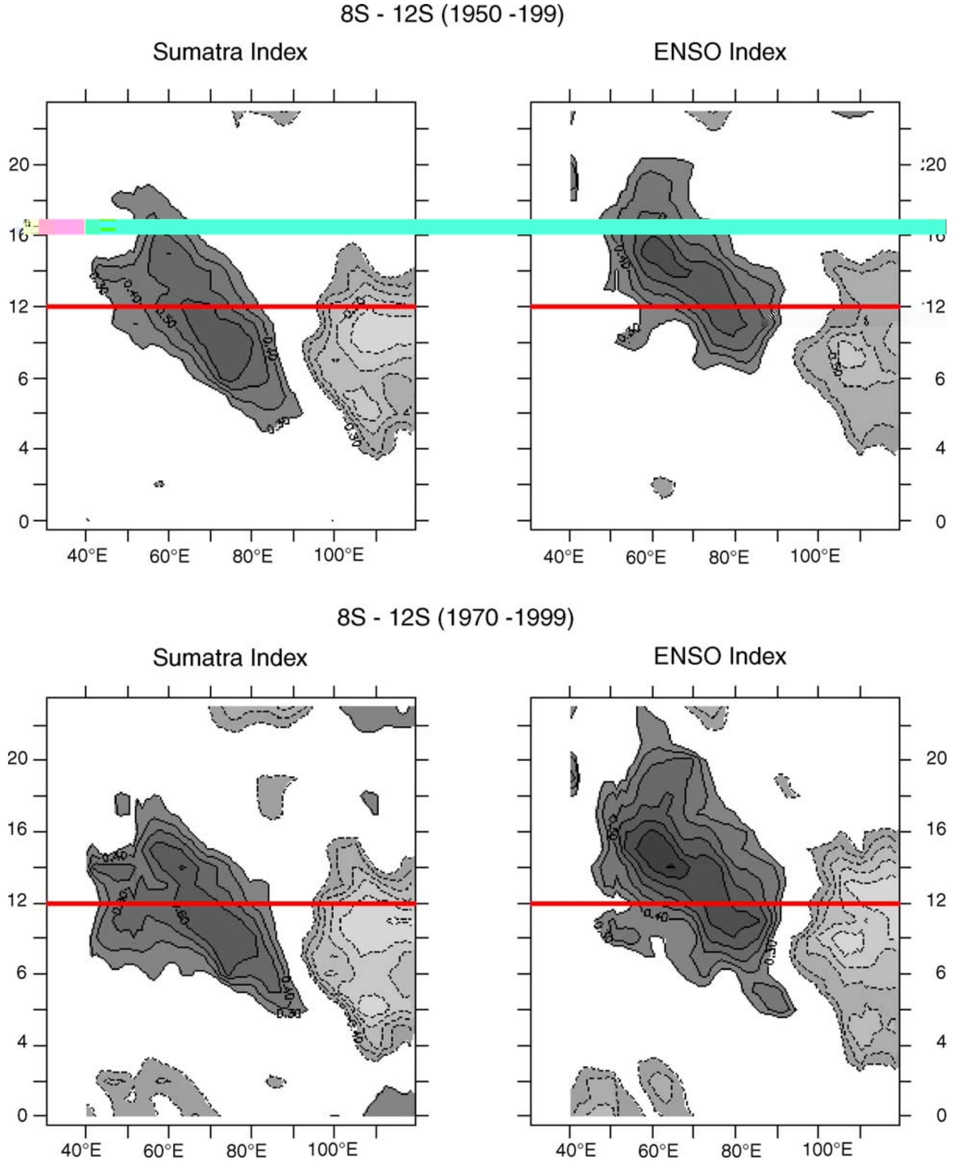

Fig. 16. Correlation between SSHA, averaged between 8°S and 12°S (top left) Sumatra index, (top right) ENSO index for 1950–1999 period, (bottom left) Sumatra index, (bottom right) ENSO index for 1970–1999 period.

warm SSTA in the western Indian Ocean, according to Behera et al. (1999), results in moisture convergence in the region above the warm SST anomalies, which in turn drives the rainfall in the surrounding regions. This hypothesis needs further examination using coupled models.

7. Decadal modulation of the subsurface influence on SST in the TIO

Decadal modulation of the thermocline depth in the northern flank of the SIO ridge and southern flank of the SIO ridge is looked in detail in this section. It should be noted here that there is strong decadal changes in observations that are integrated into the SODA. For example, XBT observations in the Indian Ocean start on a large scale in 1985; continuous satellite altimetry observations begin in 1992; and AVHRR satellite observations of SST become available in 1982. Fig. 13 shows the 11-year running correlation coefficients for the SSHA in the northern and southern flanks with the local SSTA. We have selected two typical months (September and March) to represent two distinguished structures of thermocline feedback in the TIO (Figs. 3 and 11b). A clear decadal modulation is observed for the subsurface influence on SST in both the locations during these 2 months. During September, the northern flank shows strong influence on SST throughout the study period except for the late 1970s and early 1980s. The subsurface influence on SST during March in the northern flank is strong only when the influence of subsurface on SST is weak in September (i.e. the late 1970s and early 1980s). However, the influence in the southern flank is strong throughout the study period with slight weakening during the 1950s and early 1990s in March. The subsurface influence on SST in September in the southern flank of the SIO ridge is insignificant throughout the study period except in the 1960s and 1990s.

To examine how well these modulations are associated with the major climate signals in the tropics, we present in Fig. 14 the cross-wavelet spectrum between the indices of the climate signals and the SSH for September and March. The Sumatra index and the northern ridge vary coherently during the 1960s and 1990s at quasi-biennial and quasi-pentadal time scales. It is noted that the subsurface influence on SST in September is strong during these periods (Fig. 13). The ENSO index and the southern flank of the SIO ridge vary coherently at quasi-pentadal time scales throughout the study period except during the 1950s and 1990s. This exercise shows that the decadal modulation seen in the influence of subsurface on SST at the northern and southern flanks of the SIO ridge comes mainly from IOD and ENSO modulation, respectively. However, the coherence between northern flank and ENSO index is not significant except for a short duration in the 1980s. Similarly, the coherence between the southern flank of the SIO ridge and the Sumatra index is not significant except for short durations in the 1960s and 1990s. During these decades, the feedback is stronger for the northern flank of the SIO ridge in March and for the southern flank in September (Fig. 13). Another interesting point in this analysis is that the Sumatra index leads the variations in both the northern and southern flanks of the SIO ridge, while the ENSO index lags those variations. This is because of the seasonal difference in the evolution of ENSO and IOD. Fig. 15 shows the structure of thermocline feedback on SST in the TIO during three different time periods discussed above. During the period of 1960–1969, the subsurface influence on SST is strong for the IOD season (i.e. from July to December). A similar feature of subsurface influence on SST is also observed during the period of 1980–1995. Surprisingly, the influence in the southern flank is not as well organized as in Fig. 3 for both these two decades (1960–1969; 1980–1995). It is known from previous studies (Ashok et al., 2003; Behera and Yamagata, 2003; Saji and Yamagata, 2003a) that the IOD activity was strong in the TIO during these two periods. However, during the period of 1970–1979, the subsurface influence on SST along the Sumatra coast and NIO is absent or insignificant but the influence in the southern flank region is well-organized and strong.

8. Discussion and summary

Using assimilated data from 1950 to 1999, we have shown that the subsurface influence on SST in the TIO shows strong seasonality. During the boreal summer and fall, the subsurface influence is strong both in NIO and SIO. During the rest of the year, however, it confines to the SIO, particularly to the south of 10°S. The dominant SSH interannual variability in the TIO is primarily associated with the IOD. It is also identified that the westward propagating waves are important contributors to this subsurface influence.

The observed waves that propagate westward are identified as the baroclinic Rossby waves with an intermediate phase speeds between first and second baroclinic mode phase speeds. The wave is dominantly forced by the anomalous wind stress curl in the interior TIO. Two regions of Ekman pumping are responsible for the SSH variations in the southern tropical Indian Ocean.

Since the dominant mode of interannual variability of the SSH is associated with the IOD, interannual Rossby waves north of 10°S are also dominantly associated with the IOD particularly during the IOD season. Two distinguished regions of influence of subsurface on SST are identified. IOD dominates the forcing of the off-equatorial Rossby waves, north of 10°S both in SIO and NIO, while, south of 10°S, ENSO dominance over IOD is evident after the demise of the IOD phenomenon.

Decadal modulation of the thermocline feedback is also investigated: significant decadal modulations are observed in the subsurface influence on SST in both the regions. The northern flank coherently varies with the IOD, while the southern flank varies coherently with the ENSO. It is found that northern flank thermocline feedback is strong throughout the study period except during the 1970s and the early 1980s coinciding with the IOD decadal modulation (Rao et al., 2002a; Behera and Yamagata, 2003; Ashok et al., 2003).

X02, using data from 1970 to 1999, concluded that ENSO dominantly forces the thermocline variability in the SIO. In this study, we found that IOD dominantly force the thermocline variability north of 10°S in SIO as well as in NIO. But, as shown in X02, the variability south of 10°S is dominantly forced by the ENSO-related winds after demise of the IOD in TIO. Difference in study period between X02 and the present study is found to be the one reason for this discrepancy in the conclusion. Another reason is due to X02's averaging of D20 anomalies in a wide region from 8°S to 12°S, wherein two different climate signals influence the thermocline variability in different months. Fig. 16 shows the correlation between SSHA (averaged between 8°S and 12°S) with the Sumatra index and the ENSO index for two different periods 1950–1999 and 1970–1999. When we considered the period of 1950–1999 for the analysis, the correlation is still dominant with the Sumatra index during IOD season. As stated in the present study, after the demise of IOD season, the thermocline variability in the region between 8°S and 12°S is dominantly forced by ENSO. However, if we consider only the period of 1970–1999, then we will reach the conclusion that SIO, thermocline variability south of 10°S is dominantly controlled by ENSO as in X02. Nonetheless, north of 8°S thermocline variability is still dominantly controlled by the IOD until December even during the period of 1970–1999 (not shown). As demonstrated in the present study, thermocline variability in TIO undergoes strong decadal modulation; if this fact is ignored, then contrasting results will emerge from different studies using different study periods.

The teleconnection associated with the thermocline feedback of the northern flank of the SIO ridge is also investigated. It is found that the northern flank correlates significantly with the east African rainfall during the boreal fall season. Teleconnection patterns associated with the southern flank are relatively weak during this season and therefore not considered in this study. The present study shows evidence that the SSTs that are responsible for rainfall variability over the east African rainfall are due to the subsurface feedback in the western Indian Ocean through the propagating Rossby waves. Using both the SSTA and SSHA in the eastern Indian Ocean, one may develop a prediction scheme for the east African rainfall.

We note the similarity of correlation patterns of wind stress curl with both Sumatra index (IOD) and ENSO index (ENSO) from October to December. However, our composite and partial correlation analyses suggest that the resemblance in the correlation patterns during these months could be due to the co-occurrence of IOD and ENSO in certain years. Nonetheless, it is interesting to see how these two interannual climate signals interact with each other when they both co-occur. This problem needs to be addressed further studies to better understand the relation between IOD and ENSO.

Acknowledgments

We express our gratitude to Prof. Yamagata for his constant encouragement and guidance throughout this study. We thank N.H. Saji for his help with the cross-wavelet analysis. FERRET freeware is extensively used in this study.

References

Aiki, H., Yamagata, T., 2000. Successive formation of planetary lenses in an intermediate layer. Geophys. Astrophys. Fluid Dyn. 92, 1–29.

An, S.I., Wang, B., 2000. Interdecadal change of the structure of the ENSO mode and its impact on the ENSO frequency. J. Climate 13, 2044–2055.

Annamalai, H., Murtugudde, R., Potemra, J., Xie, S.P., Liu, P., Wang, B., 2003. Coupled dynamics over the Indian Ocean: spring initiation of the zonal mode. Deep Sea Res. II 50, 2305–2330.

Ashok, K., Guan, Z., Yamagata, T., 2001. Impact of the Indian Ocean dipole on the relationship between the Indian monsoon rainfall and ENSO. Geophys. Res. Lett. 28, 4499–4502.

Ashok, K., Guan, Z., Yamagata, T., 2003. A look at the relationship between the ENSO and the Indian Ocean Dipole. J. Meteorol. Soc. Jpn. 81, 41–56.

Behera, S.K., Krishnan, S., Yamagata, T., 1999. Unusual ocean–atmosphere conditions in the tropical Indian Ocean during 1994. Geophys. Res. Lett. 26, 3001–3004.

Behera, S.K., Yamagata, T., 2003. Influence of the Indian Ocean dipole on the Southern Oscillation. J. Meteorol. Soc. Jpn. 81, 169–1777.

Birkett, C., Murtugudde, R., Allan, J.A., 1999. Indian Ocean climate event brings floods to East Africa's Lakes and the Sudd Marsh. Geophys. Res. Lett. 26, 1031–1034.

Bjerknes, J., 1969. Atmospheric teleconnections from the equatorial Pacific. Mon. Wea. Rev. 97, 163–172.

Carton, J.A., Chepurin, G., Cao, X., Giese, B.S., 2000. A simple ocean data assimilation analysis of the global upper ocean 1950–1999. J. Phys. Oceanography 30, 294–309.

Chambers, D.P., Tapley, B.D., Stewart, R.H., 1999. Anomalous warming in the Indian Ocean coincident with El Niño. J. Geophys. Res. 104, 3035–3047.

Feng, M., Meyers, G., Wijffels, S., 2001. Interannual upper ocean variability in the tropical Indian Ocean. Geophys. Res. Lett. 28 (21), 4151–4154.

Guan, Z., Yamagata, T., 2003. The unusual summer of 1994 in east Asia: IOD teleconnections. Geophys. Res. Lett. 30 (10), 1544.

Guan, Z., Ashok, K., Yamagata, T., 2003. Summertime response of the tropical atmosphere to the Indian Ocean dipole sea surface temperature anomalies. J. Meteor. Soc. Jpn. 81, 533–561.

Iizuka, S., Matsuura, T., Yamagata, T., 2000. The Indian Ocean SST dipole simulated in a coupled general circulation model. Geophys. Res. Lett. 27, 3369–3372.

Kalnay, E., Kanamitsu, M., Kistler, R., Collins, W., Deaven, D., Gandin, L., Iredell, M., Saha, S., White, G., Woollen, J., Zhu, Y., Chelliah, M., Ebisuzaki, W., Higgins, W., Janowiak, J., Mo, K.C., Ropelewski, C., Wang, J., Leetmaa, A., Reynolds, R., Jenne, R., Joseph, D., 1996. The NMC/NCAR 40-Year Reanalysis Project. Bull. Amer. Meteor. Soc. 77, 437–471.

Kumar, P.S., Unnikrishna, A.S., 1995. Seasonal cycle of temperature associated wave phenomena in the upper layers of the Bay of Bengal. J. Geophys. Res. 100, 13585–13593.

Larref, Z., Rao, S.A., Yamagata, T., 2003. Modulation of Sri Lankan Maha rainfall by the Indian Ocean dipole. Geophys. Res. Lett. 30, 35-1–35-4.

Latif, M., Barnett, T.P., 1995. Interactions of the tropical oceans. J. Climate 8, 952–964.

Latif, M., Dommenget, D., Dima, M., 1999. The role of Indian Ocean sea surface temperature in forcing east African rainfall anomalies during winter 1997/1998. J. Climate 12, 3497–3504.

Le Blanc, J.L., Boulanger, J.P., 2001. Propagation and refection of long equatorial waves in the Indian Ocean from TOPEX/POSEIDON data during the 1993–1998 period. Climate Dyn. 17, 547–557.

Masumoto, Y., Meyers, G., 1998. Forced Rossby waves. J. Geophys. Res. 103, 27589–27602.

McCreary, J.P., 1984. Equatorial beams. J. Mar. Res. 42, 395–430.

Meyers, G., 1979. Annual variation in the slope of the14 °C isotherm along the equator in the Pacific Ocean. J. Phys. Oceanography 9, 885–891.

Murtugudde, R., McCreary, J.P., Busalacchi, A.J., 2000. Oceanic processes associated with anomalous events in the Indian Ocean with relevance to 1997–1998. J. Geophys. Res. 105, 3295–3306.

Neelin, J.D., Battisti, D.S., Hirst, A.C., Jin, F.-F., Wakata, Y., Yamagata, T., Zebiak, S., 1998. ENSO theory. J. Geophys. Res. 103 (C7), 14261–14290.

Perigaud, C., Delecluse, P., 1992. Annual sea-level variations in the tropical Indian Ocean from Geosat and shallow-water simulations. J. Geophys. Res. 27, 20169–20179.

Perigaud, C., Delecluse, P., 1993. Interannual sea-level variations in the tropical Indian Ocean from Geosat and shallow-water simulations. J. Phys. Oceanography 23, 1916–1934.

Philander, S.G.H., 1990. El Nino, La Nina and the Southern Oscillation. Academic Press, San Diego, CA, 289 pp.

Rao, A.S., 1998. Rossby waves in the Bay of Bengal: observations and simulations. Ph.D. Thesis. Andhra University, Visakhapatnam, India.

Rao, S.A., Behera, S.K., Masumoto, Y., Yamagata, T., 2002a. Interannual subsurface variability in the tropical Indian Ocean with a special emphasis on the Indian Ocean dipole. Deep Sea Res. II 49, 1549–1572.

Rao, A.S., Goapalakrishna, V.V., Shetye, S.R., Yamagata, T., 2002b. On the absence of cool sea surface temperature anomalies during 1997 dipole mode event. Geophys. Res. Lett. 29, 10.1029/2001GL014645.

Rao, A.S., Yamagata, T., 2004. Abrupt termination of the Indian Ocean dipole events in response to intraseasonal disturbances. Geophys. Res. Lett. 31, L19306.

Rayner, N.A., Horton, E.B., Parker, D.E., Folland, C.K., Hackett, R.B., 1996. Version 2.2 of the Global Sea-Ice and Sea Surface Temperature Data Set, 1903–1994. Climate Research Technical Note 74. Hadley Centre for Climate Prediction and Research, Meteorological Office, London Road, Bracknell, RG12 2SY.

Saji, N.H., Goswami, B.N., Vinayachandran, P.N., Yamagata, T., 1999. A dipole mode in the tropical Indian Ocean. Nature 401, 360–363.

Saji, N.H., Yamagata, T., 2003a. Structure of SST and surface wind variability during Indian Ocean dipole mode events: COADS observations. J. Climate 16, 2735–2751.

Saji, N.H., Yamagata, T., 2003b. Inference of teleconnection patterns generated from the tropical Indian and Pacific Oceans. Climate Res. 25, 151–169.

Schiller, A., Godfrey, J.S., McIntosh, P.C., Meyers, G., Fiedler, R., 2000. Interannual dynamics and thermodynamics of the Indo-Pacific Oceans. J. Phys. Oceanography 30, 987–1012.

Schott, F.A., McCreary, J.P., 2001. The monsoon circulation of the Indian Ocean. Prog. Oceanography 51, 1–123.

Tourre, Y.M., White, W.B., 1995. ENSO signals in the global upper-ocean temperature. J. Phys. Oceanography 25, 1317–1332.

Trenberth, K.E., Hurrell, J.W., 1994. Decadal atmosphere–ocean variations in the Pacific. Climate Dyn. 9, 303–319.

Trenberth, K.E., Branstator, G.W., Karoly, D., Kumar, A., Lau, N.-C., Ropelweski, C., 1998. Progress during TOGA in understanding and modeling global teleconnections associated with tropical sea surface temperatures. J. Geophys. Res. 103, 14234–14291.

Venzke, S., Latif, M., Villwock, A., 2000. The coupled GCM ECHO-2. Part II: Indian Ocean response to ENSO. J. Climate 13, 1371–1383.

Vinayachandran, P.N., Saji, N.H., Yamagata, T., 1999. Response of the equatorial Indian Ocean to an anomalous wind event during 1994. Geophys. Res. Lett. 26, 1613–1616.

Vinayachandran, P.N., Iizuka, S., Yamagata, T., 2002. Indian Ocean dipole mode events in an Ocean General Circulation Model. Deep Sea Res. II 49, 1573–1596.

Wallace, J.M., Rasmusson, E.M., Mitchell, T.P., Kousky, V.E., Sarachik, E.S., von Storch, H., 1998. On the structure and evolution of ENSO-related climate variability in the tropical Pacific: lessons from TOGA. J. Geophys. Res. 103, 14241–14259.

Webster, P.J., Moore, A.M., Loschingg, J.P., Leben, R.R., 1999. Coupled ocean–atmosphere dynamics in the Indian Ocean during 1997–98. Nature 401, 356–360.

Woodberry, K.E., Luther, M.E., O' Brien, J.J., 1989. The winddriven seasonal circulation in the southern tropical Indian Ocean. J. Geophys. Res. 94, 17985–18002.

Xie, S.-P., Annamalai, H., Schott, F., McCreary, J.P., 2002. Structure and mechanisms of south Indian Ocean climate variability. J. Climate 15, 864–878.

Yamagata, T., Mizuno, K., Masumoto, Y., 1996. Seasonal variations in the equatorial Indian Ocean and their impact on the Lombok throughflow. J. Geophys. Res. 101, 12465–12473.

Yamagata, T., Behera, S.K., Rao, S.A., Guan, Z., Ashok, K., Saji, H.N., 2002. The Indian Ocean dipole: a physical entity. CLIVAR Exch. 24, 15–18, 20–22.

Yamagata, T., Behera, S.K., Rao, S.A., Guan, Z., Ashok, K., Saji, H.N., 2003. Comments on “dipoles, temperature gradient, and tropical climate anomalies”. Bull. Am. Meteorol. Soc. 84, 1418–1422.